JCTC Journal of Chemical Theory and Computation

Influence of Guest−Host Interactions on the Structural, Energetic, and Mössbauer Spectroscopy Properties of Iron(II)tris(2,2′-bipyridine) in the Low-Spin and High-Spin States: A Density-Functional Theory Study of the Zeolite-Y Embedded Complex

Alfredo Vargas, Andreas Hauser, and Latévi Max Lawson Daku*

Département de Chimie Physique, Université de Genève, 30 quai Ernest-Ansermet, CH-1211, Genève 4, Switzerland

Abstract: Density functional theory is applied within a supramolecular approach to the study of the guest−host interactions in $[Fe(bpy)_3]^{2+}$@Y and their influence on the structural, energetic, and ^{57}Fe Mössbauer spectroscopy properties of the encapsulated $[Fe(bpy)_3]^{2+}$ complex in the low- and high-spin states. The structures of the isolated complex and the supramolecular model used for $[Fe(bpy)_3]^{2+}$@Y were optimized in both spin-states using different generalized gradient approximation (PBE, HCTH, OLYP) and hybrid (B3LYP*, O3LYP) functionals. The results obtained are consistent with one another and show that, in either spin-state, the structure of $[Fe(bpy)_3]^{2+}$ shrinks and distorts upon encapsulation. Still, the structural changes experienced by the complex in a given spin-state remain limited, especially in that they do not lead to a substantial variation of the ^{57}Fe quadrupole splitting, whose calculated values are in very good agreement with avalaible experimental data. The decomposition of the guest−host interaction energy into its electrostatic, Pauli and orbital contributions shows that the bonding between the complex and the supercage is more electrostatic than covalent. The ability of modern functionals to accurately describe the interactions explains the remarkable consistency of the results obtained with the various functionals. In particular, although the functionals perform very differently for the determination of the high-spin/low-spin energy difference ΔE_{HL}^{el} in $[Fe(bpy)_3]^{2+}$ and $[Fe(bpy)_3]^{2+}$@Y, they consistently predict that the encapsulation entails a destabilization of the high-spin state with regard to the low-spin state of $\Delta(\Delta E_{HL}^{el}) = 2500$ cm^{-1}. Using for $[Fe(bpy)_3]^{2+}$ the CASPT2 value of $\Delta E_{HL}^{el} = 3700$ cm^{-1} [Pierloot, K.; Vancoillie, S. *J. Chem. Phys.* 2006, *125,* 124303; Pierloot, K.; Vancoillie, S. *J. Chem. Phys.* 2008, *128,* 034104], we obtain for the high-spin/low-spin energy difference in $[Fe(bpy)_3]^{2+}$@Y, a best ab initio estimate of $\Delta E_{HL}^{el} = 6200$ cm^{-1}.

1. Introduction

The increasing demand on new functional materials for use in advanced nanoscale technologies makes the control of the wide range of properties of transition metal compounds a more than ever attractive goal. In this respect, varying the environment of transition metal complexes, hence the involved guest−host interactions, proves to be an efficient means to finely tune their electronic properties, as this will be exemplified here for the title complex $[Fe(bpy)_3]^{2+}$ (bpy = 2,2′-bipyridine). This is a low-spin (LS) d^6 complex, that is, its electronic ground-state corresponds to the ligand-field $^1A_1(t_{2g}^6)$ state, while the ligand-field high-spin (HS) $^5T_2(t_{2g}^4E_g^2)$ state lies

* To whom correspondence should be addressed. E-mail: max.lawson@unige.ch.

too high in energy to become thermally populated. As in the case of the spin-crossover systems, the population of the metastable HS state can be achieved by photoexcitation, and the kinetics of the subsequent HS → LS relaxation can be followed by time-resolved absorption spectroscopy.[1] However, because of the larger HS−LS zero-point energy difference ($\Delta E^\circ_{HL} = E^\circ_{HS} - E^\circ_{LS}$), the relaxation dynamics reported for the LS [Fe(bpy)$_3$]$^{2+}$ complex are faster than for spin-crossover compounds. Thus, while the low-temperature tunnelling rate constants, $k_{HL}(T \to 0)$, are between 10^{-6} and 10^{-1} s^{-1} for spin-crossover compounds, they take on values between 10^4 and 10^8 s^{-1} for the title complex doped into a series of photophysically inert crystalline hosts.[2−5] The HS → LS relaxation is described by the theory of nonadiabatic multiphonon relaxation (see ref 1 and references therein). The quantitative analysis of the low-temperature relaxation dynamics reported for [Fe(bpy)$_3$]$^{2+}$ within this framework showed that the different environments provided by these hosts make ΔE°_{HL} vary between 2500 and 5000 cm^{-1}.[6,7]

In passing from the LS to the HS state, the metal−ligand bond length of [Fe(bpy)$_3$]$^{2+}$ increases by $\Delta r_{HL} = r_{HS} - r_{LS} \approx 0.2$ Å, and concomitantly, the molecular volume increases by $\Delta V_{HL} = V_{HS} - V_{LS} \approx 20$ Å^3.[6,8] This is caused by the promotion of two electrons from the metallic nonbonding orbital levels of octahedral t_{2g} parentage into the antibonding ones of e_g parentage. The molecular volume of the complex being larger in the HS state than in the LS state, the drastic manner in which the environment influences the HS−LS zero-point energy difference can be rationalized in terms of an internal or chemical pressure exerted by the environment of the hosts on the [Fe(bpy)$_3$]$^{2+}$ guest, which destabilizes the HS state with respect to the LS state. The concept of chemical pressure is of widespread use in solid-state physics and in solid-state chemistry as it offers an appealing parallel between the effect of the external pressure on a specific property of a material and the effect on this same property of a lattice volume variation obtained by chemical changes (see, e.g., refs 9−11). Nevertheless, as discussed in refs 12 and 13, for instance, chemical and physical pressures are not necessarily equivalent. Of special interest to us is the concept of chemical pressure that was shown by Hauser et al. to provide insight not only into the manner in which the relative energies of the ligand-field states of the title complex but also that of the complexes [M(bpy)$_3$]$^{2+}$ (M = Ru, Co) and, hence, into how their electronic properties can be tuned by guest−host interactions.[5] Still, it does not give a detailed picture of the effective interactions, which we aim at providing with the present study of [Fe(bpy)$_3$]$^{2+}$ encapsulated in the supercage of zeolite Y ([Fe(bpy)$_3$]$^{2+}$@Y).

As recently reviewed by Gol'tsov,[14] zeolites with encapsulated transition metal complexes are very convenient materials for investigating guest−host interactions and their influence on the physical and chemical properties of the encapsulated complexes. Zeolites provide well-defined rigid and stable frameworks with cavities of various sizes and shapes, so that the encapsulation of transition metal complexes in these cavities allows us to vary their environment in a controlled manner. The supercage of zeolite Y has a

diameter of about 13 Å and openings of approximatively 7.4 Å,[15] which allows the encapsulation of organometallic molecules of a similar size, such as tris(2,2′-trisbipyridine) complexes, using a ship-in-a-bottle synthesis.[16,17]

The physicochemical properties of thus synthesized zeolite-Y embedded LS [Fe(bpy)$_3$]$^{2+}$ complexes have been investigated by several research groups.[18−22] X-ray diffractometry (XRD) possibly combined with UV−vis reflectance,[18,19,21] IR,[21,22] or solid-state NMR[22] spectroscopies helped evidence the formation of the complex within the supercages of zeolite Y. ^{57}Fe Mössbauer absorption spectroscopy was employed as well. This spectroscopy is an efficient tool for probing spin crossover in iron systems.[23−27] For the title LS complex, it allows the characterization of the distortion undergone upon encapsulation. Thus, in the first-ever reported study of [Fe(bpy)$_3$]$^{2+}$@Y by Quayle et al., two samples containing 5.3 and 13 Fe ions per unit cell were investigated.[18] From the Mössbauer spectroscopy study of the sample with the low iron loading, [Fe(bpy)$_3$]$^{2+}$ was found to represent about 88% of the iron content and to be characterized by an isomer shift of $\delta = 0.63$ mm s^{-1} and a quadrupole splitting of $\Delta E_Q = 0.34$ mm s^{-1}. While this value of ΔE_Q is similar to those found for [Fe(bpy)$_3$]$^{2+}$ in other matrices, that of δ is larger than the literature value of 0.3−0.5 mm s^{-1}. This difference was ascribed to the influence of the high electron density within the zeolite lattice on the polarizable ligands.[18] The analysis of the Mössbauer spectrum of the second sample gave also [Fe(bpy)$_3$]$^{2+}$ as the dominant iron species, with an abundance of ~55%. Its Mössbauer parameters, $\delta = 0.46$ mm s^{-1} and $\Delta E_Q = 0.35$ mm s^{-1}, are in line with those observed for the complex in other environments. In an other study, Vankó et al.[20] investigated three samples wherein [Fe(bpy)$_3$]$^{2+}$ was found by Mössbauer spectroscopy to represent 38, 56, and 100% of the iron content and to be characterized by $\delta = 0.32$ mm s^{-1} and $\Delta E_Q = 0.32$ mm s^{-1}. Given that the ΔE_Q values thus determined for [Fe(bpy)$_3$]$^{2+}$@Y are very similar to those found for the complex in other matrices, it especially follows from these Mössbauer studies that the complex does not undergo major distortions upon encapsulation.[28]

Interestingly, the trigonal symmetry of the complex turns out to be preserved in the supercage. This could be inferred from the IR spectroscopy study of [Fe(bpy)$_3$]$^{2+}$@Y.[21] This is also supported by the EPR spectroscopy study of [Fe(bpy)$_3$]$^{3+}$@Y obtained by in situ oxidation, the recorded spectrum being indeed characteristic of the trigonal LS [Fe(bpy)$_3$]$^{3+}$ complex.[18] Consequently, to theoretically investigate the influence of the second coordination sphere on the properties of [Fe(bpy)$_3$]$^{2+}$ in zeolite Y, we adopted the supramolecular model of C_3 symmetry shown in Figure 1. This one consists of the complex and the surrounding Si and O atoms that define the supercage. The valence of the Si atoms has been saturated with H atoms. Finally, the orientation of the complex is such that its trigonal axis coincides with one C_3 axis of the supercage, which has an ideal T_d symmetry. As shown below, the study of this model within density functional theory (DFT)[29−33] allowed us to get major new insights into the nature of the guest−host interactions in [Fe(bpy)$_3$]$^{2+}$@Y and into their influence on the structural,

Properties of Iron(II)tris(2,2′-bipyridine)

J. Chem. Theory Comput., Vol. 5, No. 1, 2009 **99**
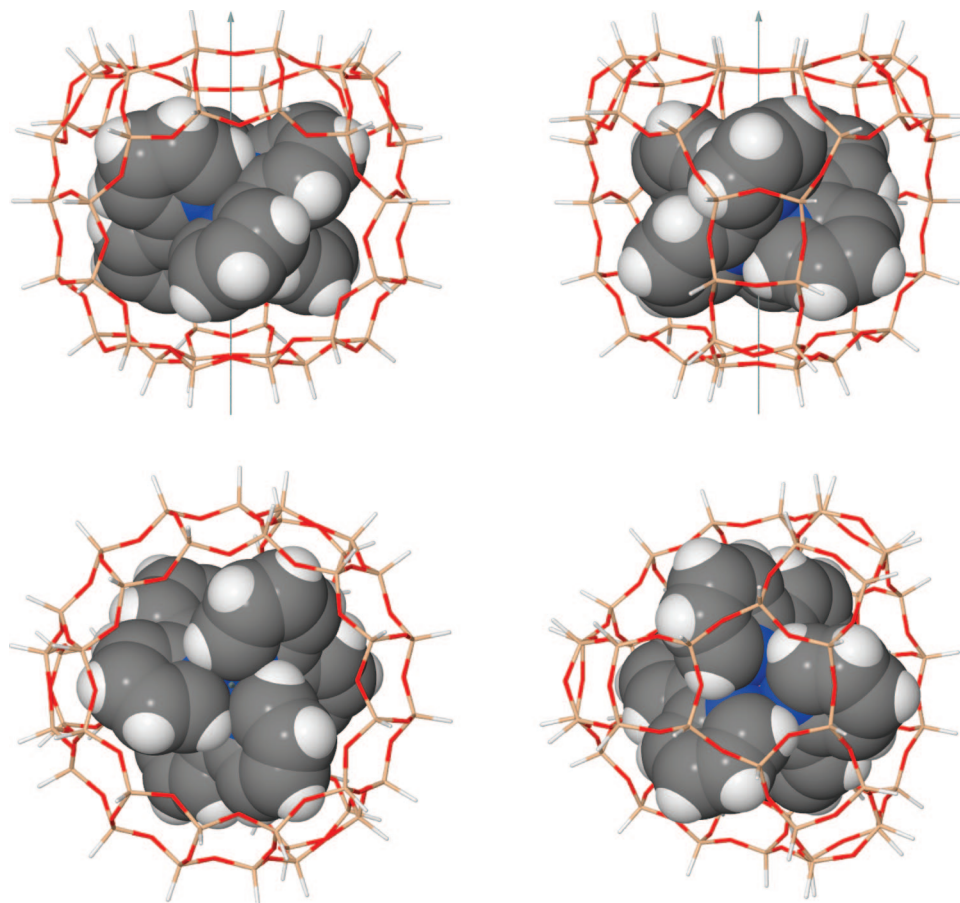
Figure 1. Supramolecular model used to investigate [Fe(bpy)$_3$]$^{2+}$@Y: the trigonal axis of [Fe(bpy)$_3$]$^{2+}$ coincides with one of the C_3 axes of the supercage that cross opposite six- and twelve-membered oxygen rings. The top drawings are side views of the models that are related to each other by a 180° rotation about the main C_3 axis; the bottom drawings are views from the top (bottom left) and from the bottom (bottom right).

energetic, and Mössbauer spectroscopy properties of the complex in the LS and in the metastable HS state.

Few studies have dealt with the experimental characterization of the metastable HS state of the zeolite-Y embedded complex. Vankó et al.[34−36] used [57]Fe Mössbauer emission spectroscopy to investigate [[57]Co(bpy)$_3$]$^{2+}$ encapsulated in the supercages of zeolite Y. They thus showed that three nucleogenic [57]Fe species are formed after the electron capture [57]Co(EC) [57]Fe nuclear decay: the LS [[57]Fe(bpy)$_3$]$^{2+}$ and LS [[57]Fe(bpy)$_3$]$^{3+}$ complexes and a HS iron(II) complex with a damaged coordination sphere. In similar investigations performed on the system [[57]Co/Mn(bpy)$_3$](PF$_6$)$_2$ by Deisenroth et al.,[3,37] Mössbauer emission spectroscopy could be used to show the formation of a fourth species, namely, the ligand-field HS [[57]Fe(bpy)$_3$]$^{2+}$ complex and to follow the dynamics of the subsequent HS → LS relaxation. The absence of the ligand-field HS state of [[57]Fe(bpy)$_3$]$^{2+}$ in the Mössbauer emission spectra of [[57]Co(bpy)$_3$]$^{2+}$@Y was therefore ascribed by Vankó et al. to the very short lifetime τ_{HS} of this state in zeolite Y, which results from the strong increase of ΔE^0_{HL} upon encapsulation and which prevents its detection with this spectroscopic technique. Nevertheless, from the time-integral Mössbauer emission spectroscopy intensity data of [[57]Co(bpy)$_3$]$^{2+}$@Y, Vankó et al. were able to determine for τ_{HS} an upper limit of 60 ns or equivalently a lower limit of 1.67×10^7 s^{-1} for $k_{HL}(T \rightarrow 0)$.[36]

2. Computational Details

The Gaussian03 program package[38] was used to optimize the geometries of the isolated [Fe(bpy)$_3$]$^{2+}$ complex, the supercage, and the [Fe(bpy)$_3$]$^{2+}$@Y model. The calculations were run with the symmetry constrained to C_3. The OLYP,[39,40] B3LYP*,[41−43] HCTH,[44] O3LYP,[45] and PBE[46,47] exchange-correlation (XC) functionals were employed in combination with the $\mathscr{G}$ basis set of Gaussian-type orbital (GTO) functions. In this basis set, the H atoms are described by the Pople double-ζ polarized 6−31G** basis set.[48,49] For the heavy atoms, the compact effective potentials (CEPs) of Stevens et al. are used to describe the atomic core electrons, while the valence electrons are described with associated GTO basis sets of double-ζ polarized quality, for the C, Si, O, and N atoms, (CEP-31G* basis set), and of triple-ζ quality for the Fe atom, (CEP-121G basis set).[50,51] The optimization calculations were performed with the default convergence criteria, and it proved necessary to resort to a large integration grid consisting of 99 radial shells and 770 angular points per shell.

To get insight into the guest−host interactions in [Fe(bpy)$_3$]$^{2+}$@Y, we have analyzed the interaction energy between the complex and the supercage using the bonding energy decomposition scheme implemented in the Amsterdam Density Functional (ADF) program package.[52,53] The

calculations were performed on the optimized OLYP/$\mathscr{G}$ geometries with the OLYP functional and the all-electron TZP basis set of triple-ζ polarized quality from the ADF Slater-type orbital (STO) basis set database, thereafter referred to as the $\mathscr{G}$ basis set. The ADF package was also used for the determination of the ^{57}Fe quadrupole splitting of the free and encapsulated [Fe(bpy)$_3$]$^{2+}$ complex. This one was derived from the electric field gradient (EFG) at the iron center obtained by scalar relativistic (SR) calculations carried out within the zeroth-order relativistic approximation (ZORA), as well as within the ZORA-4 approximation, which incorporates the small component density.[54] The EFG calculations were performed with the all-electron ZORA relativistic TZP basis set, (referred to below as the $\mathscr{J}_R$ basis set), and the OLYP and PBE functionals. In all calculations with the ADF package, we could not make use of the C_3 symmetry of the involved structures because this point group is not supported. All these calculations were therefore performed in C_1 symmetry. A high accurracy parameter "accint" of 6 was also used. Note that for the characterization of the free or embedded complex in the HS state, it was also necessary to apply electron smearing to help the calculations converge; the smearing parameter "smearq" being set to the small value of 0.003 Ha.

The Jmol program[55,56] was used for visualizing the molecular structures.

3. Results and Discussion

3.1. Characterization of [Fe(bpy)$_3$]$^{2+}$@Y in the Low-Spin State. *3.1.1. Structural Properties.* For all XC functionals used, the optimization of the structure of the isolated complex in C_3 symmetry led to an optimized geometry of D_3 symmetry. In these calculated LS geometries of [Fe(bpy)$_3$]$^{2+}$, as well as in others that are considered subsequently, the arrangement of the ligands around the iron center are characterized by the following structural parameters: the Fe$-$N and Fe$-$N$'$ metal$-$ligand bond lengths, the distance C$_2-$C$'_2$ (see Figure 2 for the atom labeling) between the pyridinyl moieties, and the angles defined in Figure 3.

The values found for these structural parameters in the optimized LS geometries of free [Fe(bpy)$_3$]$^{2+}$ are reported in Table 1, along with those found in the X-ray structure of the LS complex.[57] Note that the experimental geometry of the complex in [Fe(bpy)$_3$](PF$_6$)$_2$ is of D_3 symmetry and that we therefore verify in this case: $\theta = \theta'$ and Fe$-$N = Fe$-$N$'$, as in the case of the optimized geometries. The inspection of Table 1 shows that the calculated LS geometries are consistent with one another and in good agreement with experiment. Actually, the optimized geometries of [Fe(bpy)$_3$]$^{2+}$ tend to be slightly more expanded than the experimental one, as reflected by the somewhat larger optimized iron$-$nitrogen and C$_2-$C$'_2$ bond lengths. This discrepancy is the result of the neglect of the packing and counterion effects in our calculations performed in the gas phase.

Given the confining environment provided by the supercage of zeolite-Y, the results of the calculations performed for determining the structure of [Fe(bpy)$_3$]$^{2+}$@Y may exhibit a strong dependence on the choice of the starting geometry.
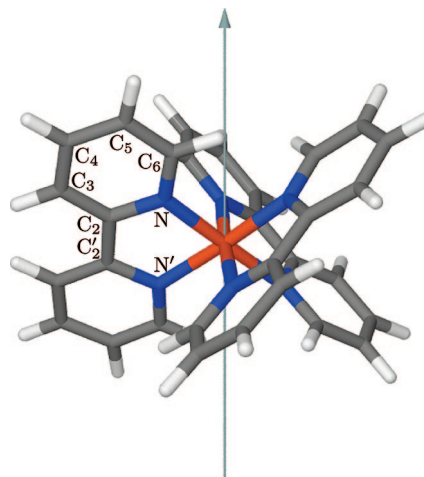
Figure 2. Atom labeling used for the complex: the atoms with primed labels belong to the equivalent pyridinyl moieties which, in the supercage, are oriented toward the six-membered ring at the bottom of the supercage (see Figure 1). Note that H$_i$ and H$'_i$ refer to the hydrogen atoms bound to atoms C$_i$ and C$'_i$, respectively ($i = 3, ..., 6$).
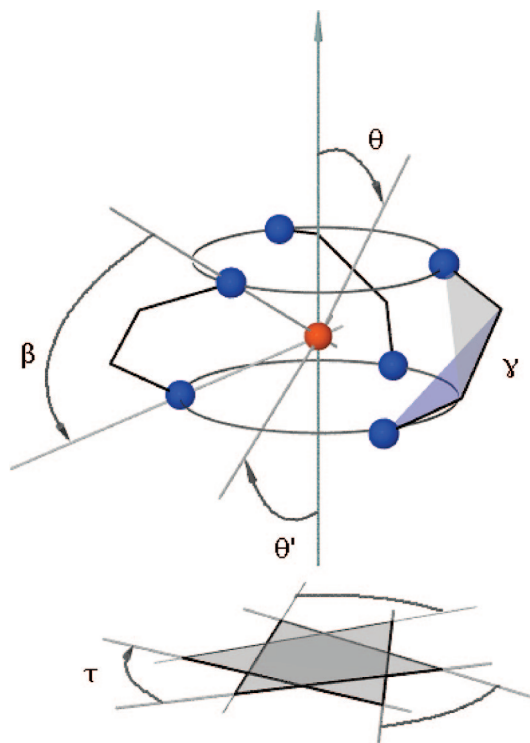

Figure 3. Angles characterizing the arrangement of the ligands around the iron center in [Fe(bpy)$_3$]$^{2+}$: $\beta = N-Fe-N'$ is the bite angle; $\gamma = N-C_2-C'_2-N'$ is the dihedral angle between the ligand moieties; τ is the twist angle; θ (respectively, θ') is the angle between the z-axis and the generator of the cone on which the nitrogen atoms labeled N (respectively, N$'$) are located.

The influence of this choice has been thoroughly investigated by carrying out a series of geometry optimizations at the OLYP/$\mathscr{G}$ level. The details of this analysis are given in the Supporting Information. The most stable optimized geometry thus obtained proves to be 11 220 cm^{-1} lower in energy than the LS reference configuration defined as the LS [Fe(bpy)$_3$]$^{2+}$ complex and the supercage taken separately and relaxed at

Table 1. Selected Bond Lengths (Å) and Angles (deg) Characterizing the Geometry of the LS [Fe(bpy)$_3$]$^{2+}$ Complex: Results of Geometry Optimization Calculations Performed on the Isolated and on the Zeolite-Y Embedded Complex[a]

		Fe−N	Fe−N′	C$_2$−C$_2'$	β	γ	τ	θ	θ'
OLYP/$\mathscr{G}$	[Fe(bpy)$_3$]$^{2+}$	1.993	1.993	1.477	81.4	3.7	54.7	58.6	58.6
	[Fe(bpy)$_3$]$^{2+}$@Y	1.956	1.986	1.473	82.2	7.5	56.9	57.7	60.3
HCTH/$\mathscr{G}$	[Fe(bpy)$_3$]$^{2+}$	1.981	1.981	1.472	81.5	3.6	54.7	58.6	58.6
	[Fe(bpy)$_3$]$^{2+}$@Y	1.951	1.976	1.468	82.3	6.0	56.9	57.8	60.1
PBE/$\mathscr{G}$	[Fe(bpy)$_3$]$^{2+}$	1.972	1.972	1.482	82.2	3.0	53.6	58.2	58.2
	[Fe(bpy)$_3$]$^{2+}$@Y	1.955	1.965	1.479	82.7	3.5	56.4	57.8	59.0
O3LYP/$\mathscr{G}$	[Fe(bpy)$_3$]$^{2+}$	2.002	2.002	1.481	81.2	3.5	54.7	58.7	58.7
	[Fe(bpy)$_3$]$^{2+}$@Y	1.966	1.994	1.476	82.0	7.2	56.7	57.8	60.1
B3LYP*/$\mathscr{G}$	[Fe(bpy)$_3$]$^{2+}$	2.010	2.010	1.490	81.4	2.7	54.7	58.4	58.4
	[Fe(bpy)$_3$]$^{2+}$@Y	1.986	2.000	1.486	82.1	3.7	55.8	57.9	59.3
exptl[b]	[Fe(bpy)$_3$](PF$_6$)$_2$	1.967	1.967	1.471	81.8	6.4	53.6	57.8	57.8

[a] The values found for these structural parameters in the X-ray structure of the LS compound [Fe(bpy)$_3$](PF$_6$)$_2$ are also given for comparison purpose. [b] Taken from ref 57.
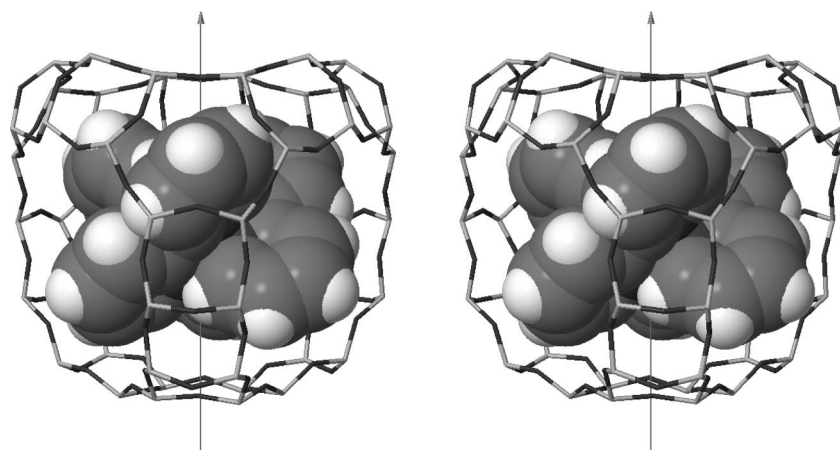
Figure 4. Stereoscopic view of the most stable structure determined for the LS [Fe(bpy)$_3$]$^{2+}$@Y system at the OLYP/$\mathscr{G}$ level (see text).

the same theoretical level. Figure 4 gives a stereoscopic view of this calculated structure that we also used as starting point in the optimization calculations performed with the other functionals for characterizing the LS [Fe(bpy)$_3$]$^{2+}$@Y system.

Figure 4 shows that the orientation of the complex within the supercage helps minimize the steric repulsion between the two subsystems. Thus, for each bipyridine, the C$_i'$−H$_i'$ (i = 3, 4, 5) and C$_3$−H$_3$ bonds face a twelve-membered window and point into the void. Likewise, the C$_4$−H$_4$ bond points toward the center of the six-membered window which, along with the previously mentioned twelve-membered window, are bisected by the average plane of the ligand. In addition, the C$_5$−H$_5$ bond points toward the twelve-membered opening on the top (i.e., the one crossed by the C_3 axis), whereas the C$_6$−H$_6$ and C$_6$−H$_6$ and C$_6'$−H$_6'$ bonds are inwardly directed. This optimal arrangement of the complex within the supercage is preserved in passing to the other calculated LS geometries of [Fe(bpy)$_3$]$^{2+}$@Y, which actually are quite close to the OLYP/$\mathscr{G}$ geometry shown in Figure 4. For all these computed geometries, selected bond lengths and angles characterizing the first coordination sphere of the encapsulated LS complex are summarized in Table 1. The comparison of these structural data with their counterparts for the isolated LS complex shows that the complex does not undergo a tremendous distortion upon encapsulation. This can also be inferred from the superposition in Figure 5A of its geometries in the gas phase and in the supercage.

Figure 5A also shows that there is a slight shrinkage of the geometry of the LS complex upon encapsulation. Thus, depending on the considered theoretical level, there is a shortening of the Fe−N and Fe−N′ bonds of 0.017−0.037 and 0.005−0.010 Å, respectively, and to a lesser extent that of the C$_2$−C$_2'$ bond of between 0.003 and 0.005 Å. Actually, for the different theoretical levels used, the decrease of the Fe−N bond length is about 2−6 times larger than the decrease of the Fe−N′ bond length. For each ligand, given that the pyridinyl moiety with the "N" labeled nitrogen atom comes the closest to the wall of the supercage, the pronounced shrinking of the Fe−N bond, as well as the accompanying noticeable decrease of the ligand cone angle θ provide an efficient means for minimizing the steric repulsion between this pyridinyl moiety and the supercage. Although the Fe−N′ bond length is far less affected by the encapsulation than the Fe−N bond length, one observes an increase of the cone angle θ' of ∼1° to ∼2°, which is made possible thanks to the space made available to the corresponding pyridinyl moiety through the twelve-membered opening that faces it. The encapsulation has also little influence on the bite angle β since the value found for the encapsulated complex differs by less than 1% from the optimal gas-phase value. For the complex to fit at best within the supercage, the twist angle τ substantially increases by about 1−3° depending on the functional used. Similarly, the dihedral

(A)

(B)

(C)
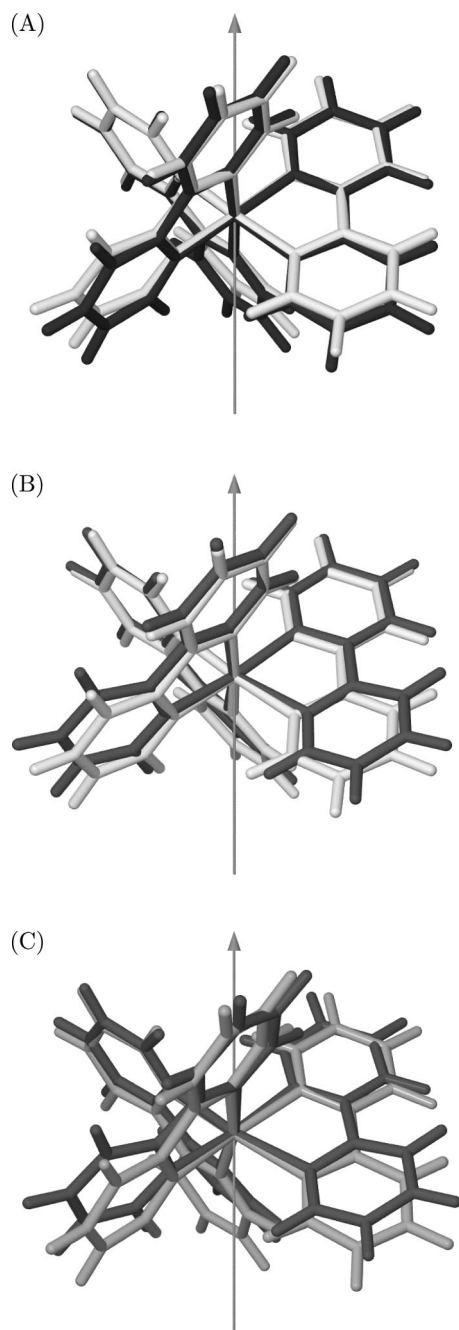
Figure 5. Superimposed geometries of $[Fe(bpy)_3]^{2+}$ showing the structural variations undergone by the complex upon a change of spin-states and/or upon encapsulation (OLYP/$\mathscr{G}$ results): (A) optimized LS geometry of the isolated complex (black) and its geometry as found in the most stable optimized LS geometry of $[Fe(bpy)_3]^{2+}$@Y (white); (B) this latter LS geometry (white) and the geometry of the complex as found in the optimized HS geometry of $[Fe(bpy)_3]^{2+}$@Y (gray); (C) geometry of the HS encapsulated complex (gray) and geometry of the isolated complex in the HS state (light gray).

angle γ increases by a factor of about 2, passing from ~3.5° to ~7°. The increase of γ is however not as large in the case of the results obtained with the PBE and B3LYP* functionals. Actually, the use of these two functionals leads to the smallest γ values for the complex both in the gas phase and in the supercage.

Finally, our results show that the geometry of the LS complex only undergoes a slight distortion upon encapsulation. For the complex, the concomitant energy change is limited as illustrated by the fact that, at the OLYP/$\mathscr{G}$ level, the passing from the relaxed geometry of the isolated complex to that of the encapsulated complex translates into a small energy increase of 1391 cm^{-1}. Similarly, the structural changes experienced by the supercage upon the inclusion of the LS complex are minimal and give rise to an increase of its energy by 3393 cm^{-1} (OLYP/$\mathscr{G}$ level). These changes are illustrated in Figure 6A by the superposition of the geometries of the supercage before and after the inclusion of the LS complex, which indeed prove to be very close. In summary, our results show that the encapsulation of the LS $[Fe(bpy)_3]^{2+}$ complex in the supercage of zeolite Y does not entail major geometric distortions neither for the complex nor for the supercage.

3.1.2. ^{57}Fe Mössbauer Quadrupole Splitting. As pointed out in the Introduction, ^{57}Fe Mössbauer spectroscopy has proven to be an efficient tool for investigating $[Fe(bpy)_3]^{2+}$@Y and especially for providing a measure of the distortion of the encapsulated complex through the determination of the quadrupole splitting ΔE_Q for the ^{57}Fe $I = 3/2$ excited nuclear state. From a computational point of view, ΔE_Q is obtained from the calculation of the eigenvalues of the traceless electric field gradient (EFG) tensor, $V_{\alpha\alpha}$ with $\alpha = x, y, z$ and $|V_{zz}| \geq |V_{yy}| \geq |V_{xx}|$, according to the relation

$$\Delta E_Q = \frac{eQV_{zz}}{2} \times \sqrt{1 + \frac{\eta^2}{3}} \tag{1}$$

where e is the electron charge, Q is the quadrupole moment of the ^{57}Fe nucleus in its $I = 3/2$ excited state,[58] where $Q = 0.14$ barn, (1 barn $= 10^{-28}$ m^2), and

$$\eta = \left| \frac{V_{xx} - V_{yy}}{V_{zz}} \right| \tag{2}$$

is the asymmetry parameter of the EFG tensor.

We proceeded to the determination of the principal values of the EFG tensor for $[Fe(bpy)_3]^{2+}$ and $[Fe(bpy)_3]^{2+}$@Y in the LS spin state by carrying out SR calculations within the ZORA and ZORA-4 approximations. For the LS $[Fe(bpy)_3]^{2+}$@Y system, the calculations performed either on the whole system or on the $[Fe(bpy)_3]^{2+}$ subsystem gave EFG components and also ΔE_Q values that agree to within less than 1%. This could be established from calculations performed at the OLYP/$\mathscr{S}_R$ and PBE/$\mathscr{S}_R$ levels using the structural description of the LS $[Fe(bpy)_3]^{2+}$@Y system obtained at the OLYP/$\mathscr{G}$ level, as well as from calculations performed at the PBE/$\mathscr{S}_R$ level using the PBE/$\mathscr{G}$ structural description of the system (data not shown). Consequently, the determination of the EFG components and hence that of the quadrupole splitting at the iron center in $[Fe(bpy)_3]^{2+}$@Y can be very accurately done without including the second coordination sphere in the calculations. That is, the influence of the environment provided by the zeolite Y on the EFG at the metallic center may be considered as being exclusively caused by the distortion of the first coordination sphere entailed by the encapsulation. The vanishing contribution of the second coordination sphere to the EFG is probably caused
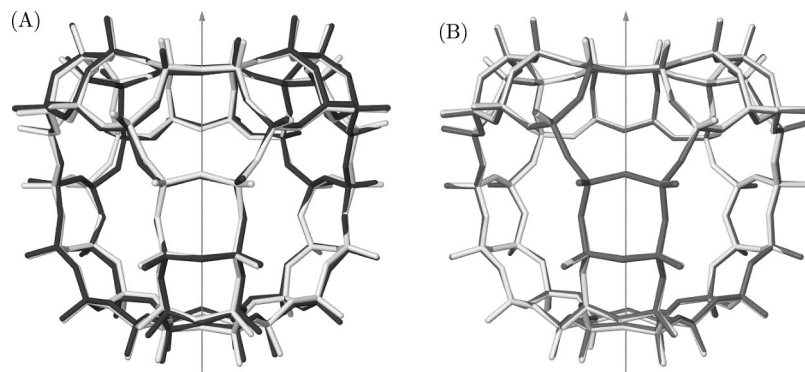
Figure 6. Superimposed geometries of the supercage showing its structural changes upon the inclusion of the LS or HS [Fe(bpy)$_3$]$^{2+}$ complex (OLYP/$\mathscr{G}$ results): (A) optimized geometry of the supercage in the gas phase (black) and its geometry as found in the optimized LS geometry of [Fe(bpy)$_3$]$^{2+}$@Y (white); (B) this latter geometry (white) and the geometry of the supercage as found in the optimized HS geometry of [Fe(bpy)$_3$]$^{2+}$@Y (gray).

by the central position of the iron atom within the supercage which has an ideal T_d symmetry. In passing to the real [Fe(bpy)$_3$]$^{2+}$@Y system, the lattice contribution to the EFG at the metallic center of [Fe(bpy)$_3$]$^{2+}$ remains vanishing because of the location of the iron atom at or in the close vicinity of a tetrahedral site of the cubic lattice. This allows the direct comparison of the theoretical results obtained for the ^{57}Fe quadrupole splitting of the encapsulated complex with the experimental ones.

Note that all EFG components and ΔE_Q values given below for [Fe(bpy)$_3$]$^{2+}$@Y in either spin-state were obtained from calculations carried out with the geometry of the encapsulated complex. This is the case for the results reported for the LS [Fe(bpy)$_3$]$^{2+}$@Y in Table 2, which also give the results obtained for the isolated LS [Fe(bpy)$_3$]$^{2+}$ complex. For both LS systems, the magnitudes of the calculated quadrupole splittings are in very good agreement with the experimental estimate of 0.3−0.4 mm s^{-1} determined for the LS complex in various media.[18,3,20−22]

The determination of the EFG components and thereof of ΔE_Q actually exhibits a negligible dependence on the choice of the functional. This could be inferred from the results of calculations performed at the OLYP/$\mathscr{S}_R$ and PBE/$\mathscr{S}_R$ levels (see Supporting Information, Table S1). Table 2 gives the results obtained at the OLYP/$\mathscr{S}_R$ level from the calculations carried out on the OLYP/$\mathscr{G}$, PBE/$\mathscr{G}$, HCTH/$\mathscr{G}$, O3LYP/$\mathscr{G}$, and B3LYP*/$\mathscr{G}$ structures. Its inspection shows that the dependence of the results on the use of the ZORA or ZORA-4 scheme is also neglibible because both schemes lead to values of the EFG components and of ΔE_Q which differ by at most ∼1%. The influence of the methods used being thus vanishingly small, we can draw the following general conclusions.

The calculated EFG tensor exhibits an axial symmetry: $V_{xx} = V_{yy}$ ($\eta = 0$), in agreement with the trigonal symmetry of the investigated systems. The calculations having been performed within C_1 symmetry, this attests to the adequacy of the integration grid that has been used (see section 2) and to the high numerical accuracy thus achieved for the determination of the EFG. The sign of V_{zz}, or equivalently that of ΔE_Q (eq 1), is found to be negative. It has not been established so far and its experimental determination requires

Table 2. Calculated Principal Values of the Electric Field Gradient Tensor, $V_{\alpha\alpha}$ ($\alpha = x, y, z$, in a.u.) and Quadrupole Splitting ΔE_Q (mm s^{-1}) at the Iron Center for [Fe(bpy)$_3$]$^{2+}$ and [Fe(bpy)$_3$]$^{2+}$@Y in the LS Manifold: Results of SR Calculations Performed at the OLYP/$\mathscr{S}_R$ Level on the Optimized HCTH/$\mathscr{G}$, O3LYP/$\mathscr{G}$, and B3LYP*/$\mathscr{G}$ Structures

		V_{zz}	$V_{xx} = V_{yy}$	ΔE_Q
OLYP/$\mathscr{G}$ geometries				
ZORA	[Fe(bpy)$_3$]$^{2+}$	−0.280	0.140	−0.397
	[Fe(bpy)$_3$]$^{2+}$@Y	−0.222	0.111	−0.313
ZORA-4	[Fe(bpy)$_3$]$^{2+}$	−0.283	0.141	−0.400
	[Fe(bpy)$_3$]$^{2+}$@Y	−0.224	0.112	−0.317
PBE/$\mathscr{G}$ geometries				
ZORA	[Fe(bpy)$_3$]$^{2+}$	−0.276	0.138	−0.390
	[Fe(bpy)$_3$]$^{2+}$@Y	−0.263	0.131	−0.372
ZORA-4	[Fe(bpy)$_3$]$^{2+}$	−0.278	0.139	−0.393
	[Fe(bpy)$_3$]$^{2+}$@Y	−0.265	0.132	−0.375
HCTH/$\mathscr{G}$ geometries				
ZORA	[Fe(bpy)$_3$]$^{2+}$	−0.283	0.141	−0.400
	[Fe(bpy)$_3$]$^{2+}$@Y	−0.241	0.120	−0.341
ZORA-4	[Fe(bpy)$_3$]$^{2+}$	−0.285	0.143	−0.403
	[Fe(bpy)$_3$]$^{2+}$@Y	−0.243	0.122	−0.344
O3LYP/$\mathscr{G}$ geometries				
ZORA	[Fe(bpy)$_3$]$^{2+}$	−0.275	0.138	−0.390
	[Fe(bpy)$_3$]$^{2+}$@Y	−0.223	0.111	−0.315
ZORA-4	[Fe(bpy)$_3$]$^{2+}$	−0.278	0.139	−0.393
	[Fe(bpy)$_3$]$^{2+}$@Y	−0.225	0.113	−0.318
B3LYP*/$\mathscr{G}$ geometries				
ZORA	[Fe(bpy)$_3$]$^{2+}$	−0.268	0.134	−0.379
	[Fe(bpy)$_3$]$^{2+}$@Y	−0.253	0.127	−0.359
ZORA-4	[Fe(bpy)$_3$]$^{2+}$	−0.270	0.135	−0.382
	[Fe(bpy)$_3$]$^{2+}$@Y	−0.256	0.128	−0.362

that the Mössbauer spectroscopy measurements be done under an applied magnetic field.

For the isolated LS complex, $\Delta E_Q \approx -0.39 \pm 0.01$ mm s^{-1}. Upon encapsulation, the magnitude of ΔE_Q decreases to an extent which proves to depend on the theoretical level used for the determination of the considered geometry of the LS [Fe(bpy)$_3$]$^{2+}$@Y system (Table 2). This evidence that the degree of distortion predicted for the encapsulated complex should be considered as varying noticeably with the functional used, although the different geometries predicted for the LS [Fe(bpy)$_3$]$^{2+}$@Y model system may be considered at first glance as being quite close to one another
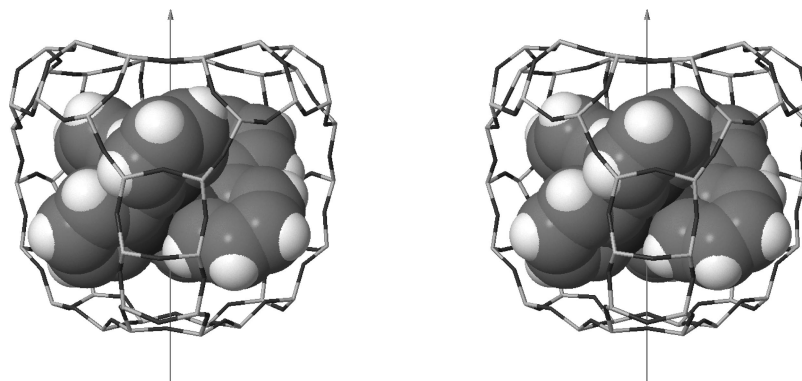
Figure 7. Stereoscopic view of the optimized OLYP/$\mathscr{G}$ geometry of the HS [Fe(bpy)$_3$]$^{2+}$@Y system.

Table 3. Selected Bond Lengths (Å) and Angles (deg) Characterizing the Geometry of the HS [Fe(bpy)$_3$]$^{2+}$ Complex: Results of Geometry Optimization Calculations Performed on the Isolated and on the Zeolite-Y Embedded Complex

		Fe−N	Fe−N′	C$_2$−C$_2'$	β	γ	τ	θ	θ'
OLYP	[Fe(bpy)$_3$]$^{2+}$	2.244	2.244	1.499	73.9	6.0	47.1	60.7	60.7
	[Fe(bpy)$_3$]$^{2+}$@Y	2.174	2.230	1.493	75.4	13.7	51.7	57.7	65.2
HCTH	[Fe(bpy)$_3$]	2.233	2.233	1.495	74.0	6.0	47.1	60.6	60.6
	[Fe(bpy)$_3$] @Y	2.177	2.222	1.490	75.4	12.3	51.8	58.0	65.0
PBE	[Fe(bpy)$_3$]$^{2+}$	2.195	2.195	1.502	75.5	5.6	47.1	59.8	59.8
	[Fe(bpy)$_3$]$^{2+}$@Y	2.160	2.181	1.499	76.5	9.0	51.3	58.3	62.8
O3LYP	[Fe(bpy)$_3$]$^{2+}$	2.237	2.237	1.498	73.9	5.4	46.9	60.6	60.6
	[Fe(bpy)$_3$]$^{2+}$@Y	2.178	2.226	1.493	75.2	12.8	51.5	57.8	65.2
B3LYP*	[Fe(bpy)$_3$]$^{2+}$	2.214	2.214	1.505	75.0	4.3	47.1	59.8	59.8
	[Fe(bpy)$_3$]$^{2+}$@Y	2.177	2.200	1.501	76.0	8.2	51.0	58.2	63.4

(Table 1). The ratio of the metal−ligand bond lengths Fe−N/Fe−N′ constitutes an immediate and relevant measure of the degree of distortion of the trigonal complex, which furthermore can be readily correlated with the values found for the quadrupole splitting.

This ratio thus takes for the isolated LS complex a value of one (1.000), as imposed by the molecular D_3 symmetry, and the results of the different EFG calculations lead to $\Delta E_Q \approx -0.39$ mm s^{-1} to within ± 0.01 mm s^{-1}. In passing to the encapsulated LS complex of C_3 symmetry, the Fe−N/Fe−N′ ratio decreases, taking the values of 0.995, 0.993, 0.987, 0.986, and 0.985 for the geometries obtained with the PBE, B3LYP*, HCTH, O3LYP, and OLYP functionals, respectively. The quadrupole splittings determined from these geometries vary monotonically with the Fe−N/Fe−N′ ratio, taking the values of $\Delta E_Q \approx -0.38$, −0.36, −0.34, −0.32, and −0.32 mm s^{-1}, respectively. That is, there is a negative correlation between the Fe−N/Fe−N′ ratio and the value ΔE_Q. Hence, as anticipated above, the quadrupole splitting ΔE_Q increases with the distortion of the complex. Finally, Vankó et al. having established that $|\Delta E_Q| \approx 0.32$ mm s^{-1} for the LS [Fe(bpy)$_3$]$^{2+}$@Y compound,[20] the observed correlation suggests that the OLYP, O3LYP, and HCTH functionals perform better for the description of the structure of the zeolite-Y embedded LS complex than the PBE and B3LYP* functionals.

3.2. Characterization in the High-Spin State.
3.2.1. Structural Properties. The optimization calculations performed with the Gaussian package for characterizing [Fe(bpy)$_3$]$^{2+}$ and [Fe(bpy)$_3$]$^{2+}$@Y in the ligand-field HS $^5T_2(t_{2g}^4 E_g^2)$ state led to their characterization in the HS ^5A trigonal component. The other trigonal HS component of ^5E

symmetry is not available through such calculations. This indeed requires the use of fractional occupation numbers, which actually is not implemented in the current version of the Gaussian package, except as an intermediate step in the self-consistent field convergence strategy. For the two investigated systems, given that the $^5A \leftrightarrow {}^5E$ change of states consists mainly in an electronic rearrangement within the nonbonding metallic levels of octahedral Fe(t_{2g}) parentage, one can assume that the HS components are close in energy and that they exhibit similar geometries, as effectively shown for the isolated complex in a previous study.[6] The characterization thus achieved for the structures and the energetics of [Fe(bpy)$_3$]$^{2+}$ and [Fe(bpy)$_3$]$^{2+}$@Y in the ^5A state therefore extends to the ^5E component of the HS state as well.

For the HS [Fe(bpy)$_3$]$^{2+}$@Y system, the optimization calculations were performed first with the OLYP functional. This led to an optimized geometry wherein the orientation of the complex within the supercage is identical to the optimal one observed in the most stable structure of LS [Fe(bpy)$_3$]$^{2+}$@Y (see Figure 7). We therefore did not carry out further calculations for investigating the influence of the choice of the initial geometry on the outcome of the optimization calculations and used the optimized OLYP/$\mathscr{G}$ geometry of HS [Fe(bpy)$_3$]$^{2+}$@Y as starting point in the subsequent minimizations performed with the other functionals. As for the isolated complex, the calculations performed within C_3 led to final HS geometries of effective D_3 symmetry.

The selected bond lengths and angles reported in Table 3 for the isolated (respectively, encapsulated) complex show that the optimized HS geometries of [Fe(bpy)$_3$]$^{2+}$ (respectively, [Fe(bpy)$_3$]$^{2+}$@Y) are consistent with one another. For

the isolated complex, these structural data also compare very well with those previously reported for $[Fe(bpy)_3]^{2+}$ in the HS state.[6] As for $[Fe(bpy)_3]^{2+}$@Y, the optimized HS geometries resemble the OLYP/$\mathscr{G}$ one shown in Figure 7. In both cases, the major structural change undergone by $[Fe(bpy)_3]^{2+}$ upon the LS → HS change of spin-states is the lengthening of the iron–ligand bond, which follows from the promotion of two electrons from the nonbonding metallic levels of $Fe(t_{2g})$ parentage into the antibonding metallic level of $Fe(e_g)$ parentage. The comparison of Tables 1 and 3 shows that this increase, Δr_{HL}, of the iron–nitrogen distance in $[Fe(bpy)_3]^{2+}$ and in $[Fe(bpy)_3]^{2+}$@Y is on the average between 0.20 and 0.25 Å, depending on the functional. For the isolated complex, the large increase of the metal–ligand bond length is accompagnied by a slight lengthening of the $C_2–C_2'$ bond of ~0.02 Å and by relatively large variations of the angles β, γ, τ, and $\theta = \theta'$, which reflect the structural changes and spatial rearrangements undergone by the ligands upon the LS → HS conversion, so as to maintain the metal–ligand bonding interactions optimal. For the encapsulated complex, concomitant with the increase of the metal–ligand bonds, there is likewise a ~0.02 Å increase of the $C_2–C_2'$ bond length and significant changes in the values of the angular parameters β, γ, τ, and θ'; the value of the cone angle θ remaining close to its LS value. The structural changes thus undergone by the ligands can also be seen in Figure 5B. Interestingly, the large expansion experienced by the guest complex upon the LS → HS spin-state conversion hardly affects the structure of the supercage because of the rigidity of this host. This is illustrated in Figure 6B by the nearly perfect match of the OLYP/$\mathscr{G}$ LS and HS geometries of the supercage; the latter being less stable than the former by 312 cm^{-1} only.

Inspection of Table 3 shows that the geometry of the HS $[Fe(bpy)_3]^{2+}$ complex contracts upon encapsulation, as exemplified in Figure 5C by the superposition of the OLYP/$\mathscr{G}$ geometries of the HS complex in the gas phase and in the supercage of zeolite Y. Depending on the considered theoretical level, this shrinkage of the geometry of the HS complex translates into a decrease of the Fe–N and Fe–N′ bond lengths of about 0.04–0.07 and 0.01 Å, respectively, and also into a small decrease of the $C_2–C_2'$ bond length (<0.01 Å). The angular parameters used to describe the arrangement of the ligands in the HS geometry are also noticeably influenced by the encapsulation. The cone angle θ thus decreases by 1.5–3.0°, while the other cone angle, θ', increases by 3.0–4.6°. Concurrently, the bite angle β and the twist angle τ increase by 1.0–1.5° and 3.9–4.7°, respectively. The dihedral angle γ also substantially increases by 6.3–7.7°, except in the case of the results obtained with the PBE and B3LYP* functionals, wherein far smaller increases of 3.5° and 3.9°, respectively, are predicted for γ. As previously observed during the investigation of the structural properties of the LS complex, the use of PBE and B3LYP* functionals leads to the smallest predicted γ values for the isolated and the encapsulated HS complex.

These structural changes experienced by the HS complex to fit at best within the supercage are similar to but more pronounced than those undergone by the LS complex upon

Table 4. Calculated Principal Values of the Electric Field Gradient Tensor, $V_{\alpha\alpha}$ ($\alpha = x$, y, z, in au), and Quadrupole Splitting ΔE_Q (mm s^{-1}) at the Iron Center for $[Fe(bpy)_3]^{2+}$ and $[Fe(bpy)_3]^{2+}$@Y in the ^5E Component of the HS State: Results of SR Calulations Performed at the OLYP/$\int_R$ Level[a]

		V_{zz}	$V_{xx} = V_{yy}$	ΔE_Q
OLYP/$\mathscr{G}$ geometries				
ZORA	$[Fe(bpy)_3]^{2+}$	0.938	−0.469	1.328
	$[Fe(bpy)_3]^{2+}$@Y	0.989	−0.495	1.400
ZORA-4	$[Fe(bpy)_3]^{2+}$	0.936	−0.468	1.324
	$[Fe(bpy)_3]^{2+}$@Y	0.986	−0.493	1.396
PBE/$\mathscr{G}$ geometries				
ZORA	$[Fe(bpy)_3]^{2+}$	0.938	−0.469	1.327
	$[Fe(bpy)_3]^{2+}$@Y	0.966	−0.483	1.367
ZORA-4	$[Fe(bpy)_3]^{2+}$	0.936	−0.468	1.324
	$[Fe(bpy)_3]^{2+}$@Y	0.963	−0.482	1.363
HCTH/$\mathscr{G}$ geometries				
ZORA	$[Fe(bpy)_3]^{2+}$	0.946	−0.473	1.338
	$[Fe(bpy)_3]^{2+}$@Y	0.991	−0.495	1.402
ZORA-4	$[Fe(bpy)_3]^{2+}$	0.943	−0.472	1.334
	$[Fe(bpy)_3]^{2+}$@Y	0.988	−0.494	1.398
O3LYP/$\mathscr{G}$ geometries				
ZORA	$[Fe(bpy)_3]^{2+}$	0.941	−0.471	1.332
	$[Fe(bpy)_3]^{2+}$@Y	0.991	−0.495	1.402
ZORA-4	$[Fe(bpy)_3]^{2+}$	0.939	−0.470	1.328
	$[Fe(bpy)_3]^{2+}$@Y	0.988	−0.494	1.397
B3LYP*/$\mathscr{G}$ geometries				
ZORA	$[Fe(bpy)_3]^{2+}$			
	$[Fe(bpy)_3]^{2+}$@Y	0.968	−0.484	1.369
ZORA-4	$[Fe(bpy)_3]^{2+}$			
	$[Fe(bpy)_3]^{2+}$@Y	0.965	−0.483	1.366

[a] Note that we were not able to make converge the calculations performed on the B3LYP*/$\mathscr{G}$ geometry of $[Fe(bpy)_3]^{2+}$.

encapsulation. This clearly follows from the fact that the molecular volume of $[Fe(bpy)_3]^{2+}$ is larger in the HS state than in the LS state. The more pronounced distortion undergone by the complex in the HS state upon encapsulation can also be inferred from the comparison of Figure 5, parts A and C, which show the superimposed OLYP/$\mathscr{G}$ geometries of the isolated and of the encapsulated complex in the LS and HS states, respectively. On a similar note, the passing from the OLYP/$\mathscr{G}$ geometry of the isolated complex to the one of the encapsulated complex is associated to an energy increase of 3740 cm^{-1} for the complex in the HS state, whereas this energy increase was found to amount to 1391 cm^{-1} only for the complex in the LS state.

3.2.2. ^{57}Fe Mössbauer Quadrupole Splitting. The SR calculations performed with the ADF package within C_1 for the determination of the EFG at the iron site of the isolated or the encapsulated HS $[Fe(bpy)_3]^{2+}$ complex converged all to the ^5E trigonal component of the HS state. The results of these calculations carried out at the OLYP/$\int_R$ level on the geometries of the free and of the encapsulated HS complex are summarized in Table 4. Note that the choice of the functional proves to have little influence on the results since the EFG calculations similarly performed at the PBE/$\int_R$ level on the PBE/$\mathscr{G}$ and OLYP/$\mathscr{G}$ geometries gave results that differ by 2% at most from those similarly obtained with the OLYP functional.

There is a fairly good consistency among the results given in Table 4. The calculated EFG tensors exhibit an axial symmetry ($V_{xx} = V_{yy}$), in agreement with the trigonal

106 *J. Chem. Theory Comput., Vol. 5, No. 1, 2009*

Vargas et al.

symmetry of the investigated system. The sign of V_{zz}, hence that of ΔE_Q, is found to be positive and was not experimentally determined so far. Further inspection of Table 4 shows that $\Delta E_Q \approx 1.33$ mm s^{-1} for the isolated complex in the ^{5}E state and that it increases in passing to the [Fe(bpy)$_3$]$^{2+}$@Y system in the ^{5}E state, as a consequence of the distortion entailed by the encapsulation. As previously noticed for the LS complex, this increase of ΔE_Q upon encapsulation depends on the XC functional used for optimizing the considered HS geometry of the [Fe(bpy)$_3$]$^{2+}$@Y system. That is, the degree of distortion predicted for the encapsulated complex both in the LS and in the HS state depends on the functional used.

The ratio Fe−N/Fe−N′ gives a measure of the distortion of the trigonal [Fe(bpy)$_3$]$^{2+}$ complex: the smaller it is, the more distorted the geometry of the complex. It takes the values 0.990, 0.990, 0.980, 0.978, and 0.975 for the HS geometries of [Fe(bpy)$_3$]$^{2+}$@Y obtained with the PBE, B3LYP*, HCTH, O3LYP, and OLYP, respectively. Meanwhile, for the encapsulated complex in the ^{5}E state the calculated values of the quadrupole splitting are $\Delta E_Q \approx 1.37$ for the PBE and B3LYP* geometries, and $\Delta E_Q \approx 1.40$ for the HCTH, O3LYP, and OLYP geometries. For [Fe(bpy)$_3$]$^{2+}$@Y in the LS state, we could infer from the comparison of the calculated and experimental values of ΔE_Q that the HCTH, O3LYP, and OLYP probably perform better for the description of the structure of the encapsulated LS complex than the PBE and B3LYP* functionals. Given that the distortions predicted for the encapsulated complex in the HS state follow the same trend as the one observed in the LS state, this conclusion can actually be extended to the description of the geometry of the encapsulated HS complex. That is, the HCTH, O3LYP, and OLYP functionals very likely perform better for the description of the structure of the encapsulated complex in either spin state than the PBE and B3LYP* functionals.

The above results and their discussion are valid for [Fe(bpy)$_3$]$^{2+}$ and [Fe(bpy)$_3$]$^{2+}$@Y in the ^{5}E component of the HS state only. For the determination of the EFG tensors of both systems in the ^{5}A state, we were not able to make converge the calculations performed within C_1 to this component of the HS state. For the isolated complex, we nevertheless could do so by carrying out the calculations with the molecular symmetry constrained to the effective D_3 symmetry and the occupations of the Kohn−Sham levels appropriately chosen (see ref 6). These calculations performed on all the available HS geometries of [Fe(bpy)$_3$]$^{2+}$ at the OLYP/$\mathcal{J}_R$ level gave ^{57}Fe ΔE_Q values of between −2.69 and −2.66 mm s^{-1}, depending on the considered geometry. The quadrupole splitting of the encapsulated complex in the ^{5}A state obviously deviates from this gas-phase value of about −2.7 mm s^{-1}. However, as observed for [Fe(bpy)$_3$]$^{2+}$ in the LS and in the HS ^{5}E state, it should remain close to this value because the HS geometries of the complex in the gas phase and in the supercage stay close. The ^{5}E → ^{5}A internal conversion mainly involves an electronic rearrangement within the metallic levels of non-bonding octahedral Fe(t_{2g}) parentage. As pointed out by Lawson Daku et al.,[6] this change of states translates into

the transfer of electron density from the *xy*-plane to along the trigonal *z*-axis, which explains the change of sign and of magnitude found for ΔE_Q in passing from the ^{5}E to the ^{5}A state.

The Mössbauer parameters of the HS complex have been experimentally determined by Deisenroth et al. from the Mössbauer emission spectroscopy study of [^{57}Co/Mn(bpy)$_3$](PF$_6$)$_2$.[3] In this matrix, they measured for the nucleogenic HS [^{57}Fe(bpy)$_3$]$^{2+}$ complex a quadrupole splitting of $|\Delta E_Q| = 1.17$ mm s^{-1}. The ΔE_Q values calculated for the complex in the ^{5}E state are in fairly good agreement with this value. We can therefore conclude that the ^{5}E state is the lowest-lying component of the HS state of the complex doped into [Co(bpy)$_3$](PF$_6$)$_2$. For the isolated complex, note that the two components of the HS state were shown to be nearly degenerate and that its molecular volume was shown to be slightly larger in the ^{5}A state ($\sim$22 Å^3) than in the ^{5}E state ($\sim$20 Å^3).[6] Consequently, on the basis of this molecular volume difference, the fact that the ^{5}E state is found to be the lowest-lying HS component of [Fe(bpy)$_3$]$^{2+}$ doped into [Co(bpy)$_3$](PF$_6$)$_2$ can be ascribed to the chemical pressure experienced by the complex which destabilizes the ^{5}A state with regard to the ^{5}E state. Note that this energy ordering of the trigonal components of the HS state: E(^{5}E) $\lesssim$ E(^{5}A), is probably the same for [Fe(bpy)$_3$]$^{2+}$ in the confining environment provided by the supercage of zeolite Y.

3.3. High-Spin/Low-Spin Energy Difference. *3.3.1. Determination of the Change in the Spin-State Energetics upon Encapsulation and of the Experienced Chemical Pressure.* The large number of atoms (229) of the model system devised for investigating the guest−host interactions in [Fe(bpy)$_3$]$^{2+}$@Y precludes the use of computationally demanding high-level ab initio methods. In contrast, with a computational cost formally identical to that of the Hartree−Fock method, DFT methods can efficiently be applied to the study of such large systems. However, although they perform quite well for the study of numerous properties of transition metal complexes,[59] they tend to dramatically fail when it comes to the accurate evaluation of the relative energies of the different spin-states of these systems.[6,7,60−76] This failure of the current density-functional approximations manifests itself in the present case by the large spread of the calculated values of the HS−LS electronic energy difference, ΔE_{HL}^{el}, in [Fe(bpy)$_3$]$^{2+}$ and in [Fe(bpy)$_3$]$^{2+}$@Y, which are given in Table 5A.

These values were obtained from the results of the optimization calculations performed with the Gaussian package as the energy difference between the LS ^{1}A state and the ^{5}A trigonal component of the HS state, to which the results obtained using Gaussian are restricted. They range from −811 to 10087 cm^{-1} for [Fe(bpy)$_3$]$^{2+}$ and from 1941 to 12004 cm^{-1} for [Fe(bpy)$_3$]$^{2+}$@Y. The very various performances thus exhibited by the different XC functionals with regard to the determination of ΔE_{HL}^{el} and, more generally, with regard to the issue of the spin-state energetics in transition metal complexes, have been discussed in details by different authors (see, for instance, refs 6, 61, 64, 65, 68, 70, and 74). A further discussion of this delicate issue is beyond the scope of the present study. We rather focus on

the change $\Delta(\Delta E_{HL}^{el})$ in ΔE_{HL}^{el} upon encapsulation, which is given by

$$\Delta(\Delta E_{HL}^{el}) = \Delta E_{HL}^{el}[Y] - \Delta E_{HL}^{el}[\varnothing] \qquad (3)$$

In the above equation, we introduce the notation $X[\varnothing]$ and $X[Y]$ to refer to the values of a quantity X for $[Fe(bpy)_3]^{2+}$ in the gas phase and in the supercage of zeolite Y, respectively. The values found for $\Delta(\Delta E_{HL}^{el})$ are summarized in Table 5B. There is a remarkably good consistency between these values, which are positive and spread over the narrow range of $1917-2934$ cm^{-1}. The positive values show that the HS state is destabilized with regard to the LS state upon encapsulation. Their convergence can be related to the fact that the choice of the functional tends to have a weak influence on the difference of two ΔE_{HL}^{el} values (see ref 70). In the present case, it also demonstrates that the different functionals tend to perform equally well for the evaluation of the influence of the guest−host interactions in $[Fe(bpy)_3]^{2+}@Y$ on the HS−LS energy difference, although they perform very differently for the calculation of this energy difference.

$\Delta(\Delta E_{HL}^{el})$ can be divided into three contributions: $\Delta E_{HL}^{dist}\{Fe\}$, $\Delta E_{HL}^{dist}\{Y\}$, and ΔE_{HL}^{int}. $\Delta E_{HL}^{dist}\{Fe\}$ is the energy difference

$$\Delta E_{HL}^{dist}\{Fe\} = E_{HS}^{dist}\{Fe\} - E_{LS}^{dist}\{Fe\} \qquad (4)$$

where $E_{LS}^{dist}\{Fe\}$ (respectively, $E_{HS}^{dist}\{Fe\}$) is the energy required to bring the isolated complex in the LS (respectively, HS) state from its relaxed geometry to its distorted geometry at the minimum of $[Fe(bpy)_3]^{2+}@Y$ in the LS (respectively, HS) state. $\Delta E_{HL}^{dist}\{Y\}$ is for the supercage the counterpart of $\Delta E_{HL}^{dist}\{Fe\}$ for the complex.

$$\Delta E_{HL}^{dist}\{Y\} = E_{HS}^{dist}\{Y\} - E_{LS}^{dist}\{Y\} \qquad (5)$$

where $E_{LS}^{dist}\{Y\}$ (respectively, $E_{HS}^{dist}\{Y\}$) is the energy needed to bring the supercage from its relaxed geometry to its geometry after the inclusion of $[Fe(bpy)_3]^{2+}$ in the LS (respectively, HS) state. The contributions $\Delta E_{HL}^{dist}\{Fe\}$ and $\Delta E_{HL}^{dist}\{Y\}$ sum up to a global geometric distortion term, ΔE_{HL}^{dist}.

The last contribution ΔE_{HL}^{int} to $\Delta(\Delta E_{HL}^{el})$ is the change in the guest−host interaction energy upon the LS → HS change of spin-states. It is given by

$$\Delta E_{HL}^{int} = E_{HS}^{int} - E_{LS}^{int} \qquad (6)$$

where E_{LS}^{int} (respectively, E_{HS}^{int}) is the interaction energy between the supercage and the guest complex in the LS (respectively, HS) state at the minimum of the whole system. The values found at the different theoretical levels for ΔE_{HL}^{dist} and $\Delta E_{HL}^{int} = \Delta(\Delta E_{HL}^{el}) - \Delta E_{HL}^{dist}$ are summarized in Table 5, along with the values found for $\Delta E_{HL}^{dist}\{Fe\}$ and $\Delta E_{HL}^{dist}\{Y\}$.

Of the two contributions, ΔE_{HL}^{dist} and ΔE_{HL}^{int}, to $\Delta(\Delta E_{HL}^{el})$, ΔE_{HL}^{dist} is the one responsible for the observed dispersion of ~ 1000 cm^{-1} in the calculated $\Delta(\Delta E_{HL}^{el})$ values. The values found for ΔE_{HL}^{int} indeed exhibit a remarkably weak to negligible dependence on the theoretical level used and average to $\Delta E_{HL}^{int} \approx 1300$ cm^{-1}. Meanwhile, the values found for ΔE_{HL}^{dist} range from 671 to 1593 cm^{-1} depending on the functional used. Inspection of Table 5 also shows that $\Delta E_{HL}^{dist}\{Fe\}$ is the major contribution to ΔE_{HL}^{dist}, with $\Delta E_{HL}^{dist}\{Y\}$ being 4 to 7 times smaller than $\Delta E_{HL}^{dist}\{Fe\}$. The small positive values found for $\Delta E_{HL}^{dist}\{Y\}$ show that the slight structural changes of the supercage in $[Fe(bpy)_3]^{2+}@Y$ entailed by the LS → HS change of spin-states and the concomitant expansion of the $[Fe(bpy)_3]^{2+}$ guest translate only into a weak destabilization of the host.

The geometric changes undergone by $[Fe(bpy)_3]^{2+}$ upon encapsulation are more pronounced in the HS state than in the LS state. The fact that the calculated values of $\Delta E_{HL}^{dist}\{Fe\}$ are positive (i.e., $E_{LS}^{dist}\{Fe\} < E_{HS}^{dist}\{Fe\}$) shows that these changes are also more destabilizing in the HS state than in the LS state. Figure 8 gives the plots of $E_{LS}^{dist}\{Fe\}$ and $E_{HS}^{dist}\{Fe\}$ against the ratios $\xi_{LS} = r_{LS}[Y]/r_{LS}[\varnothing]$ and $\xi_{HS} = r_{HS}[Y]/r_{HS}[\varnothing]$, respectively, where r_Γ designates the average iron−nitrogen bond length in the Γ manifold ($\Gamma = $ LS, HS).

One notes in Figure 8 that (a) $E_{\Gamma}^{dist}\{Fe\}$ increases with decreasing ξ_Γ ($\Gamma = $ LS, HS) and (b), regardless of the considered spin-state, the calculated values of ξ_Γ decrease in the order: PBE > B3LYP* > HCTH > O3LYP > OLYP. This ordering is also the one found for the LS and HS values of the ratio Fe−N/Fe−N′ in $[Fe(bpy)_3]^{2+}@Y$, which gives a measure of the predicted distortion of the geometry of the encapsulated complex: the smaller the Fe−N/Fe−N′ ratio, the more distorted the geometry of $[Fe(bpy)_3]^{2+}$ (see above). Consequently, for a given functional, ξ_Γ is a relevant measure of both the shrinkage and the distortion predicted for the geometry of $[Fe(bpy)_3]^{2+}$ in the Γ state upon encapsulation.

***Table 5.*** Spin-State Energetics: Calculated Values (cm^{-1}) of (A) the HS−LS Electronic Energy Difference ΔE_{HL}^{el} in $[Fe(bpy)_3]^{2+}$ and in $[Fe(bpy)_3]^{2+}@Y$; (B) the Change $\Delta(\Delta E_{HL}^{el})$ in ΔE_{HL}^{el} upon Encapsulation; (C) the Contributions ΔE_{HL}^{int} and ΔE_{HL}^{dist} to $\Delta(\Delta E_{HL}^{el})$; and (D) the Terms $\Delta E_{HL}^{dist}\{Fe\}$ and $\Delta E_{HL}^{dist}\{Y\}$ into which ΔE_{HL}^{dist} Divides

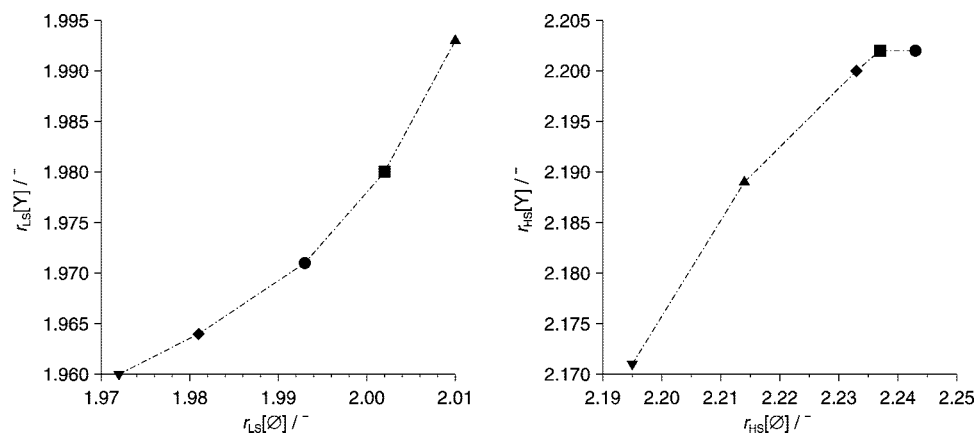|	PBE/$\mathscr{G}$	B3LYP*/$\mathscr{G}$	HCTH/$\mathscr{G}$	O3LYP/$\mathscr{G}$	OLYP/$\mathscr{G}$
	(A) HS−LS electronic energy difference ΔE_{HL}^{el}				
$[Fe(bpy)_3]^{2+}$	+10 087	+3849	+141	−811	+3660
$[Fe(bpy)_3]^{2+}@Y$	+12 004	+5925	+2687	+1941	+6594
	(B) Change in ΔE_{HL}^{el} upon encapsulation				
$\Delta(\Delta E_{HL}^{el})$	+1917	+2076	+2546	+2752	+2934
	(C) $\Delta(\Delta E_{HL}^{el}) = \Delta E_{HL}^{int} + \Delta E_{HL}^{dist}$				
ΔE_{HL}^{int}	+1246	+1267	+1621	+1286	+1331
ΔE_{HL}^{dist}	+671	+809	+925	+1466	+1593
	(D) $\Delta E_{HL}^{dist} = \Delta E_{HL}^{dist}\{Fe\} + \Delta E_{HL}^{dist}\{Y\}$				
$\Delta E_{HL}^{dist}\{Fe\}$	+583	+679	+571	+1181	+1291
$\Delta E_{HL}^{dist}\{Y\}$	+88	+130	+354	+285	+312
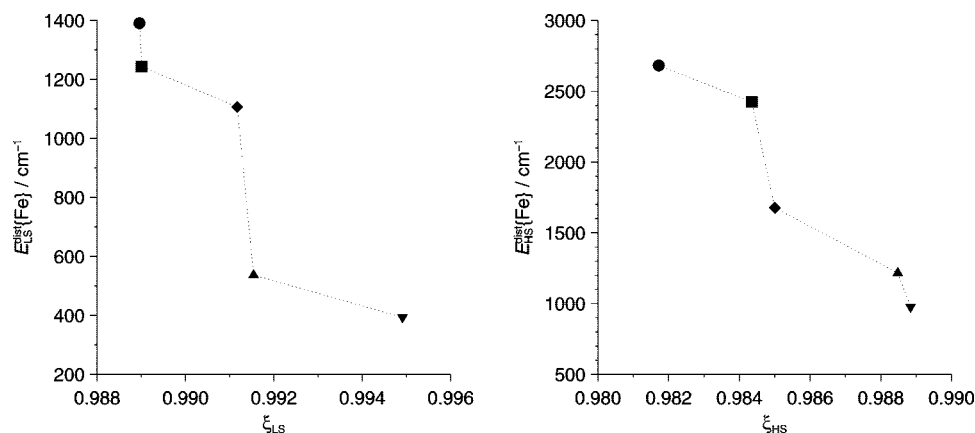
Figure 8. Plots of $E_{LS}^{dist}\{Fe\}$ against ξ_{LS} (left) and of $E_{HS}^{dist}\{Fe\}$ against ξ_{HS} (right) for the different XC functionals used: PBE/$\mathscr{G}$ (▼), B3LYP*/$\mathscr{G}$ (▲), HCTH/$\mathscr{G}$ (◆), O3LYP/$\mathscr{G}$ (■), and OLYP/$\mathscr{G}$ (●) results (lines serve to highlight the trends among the functionals).
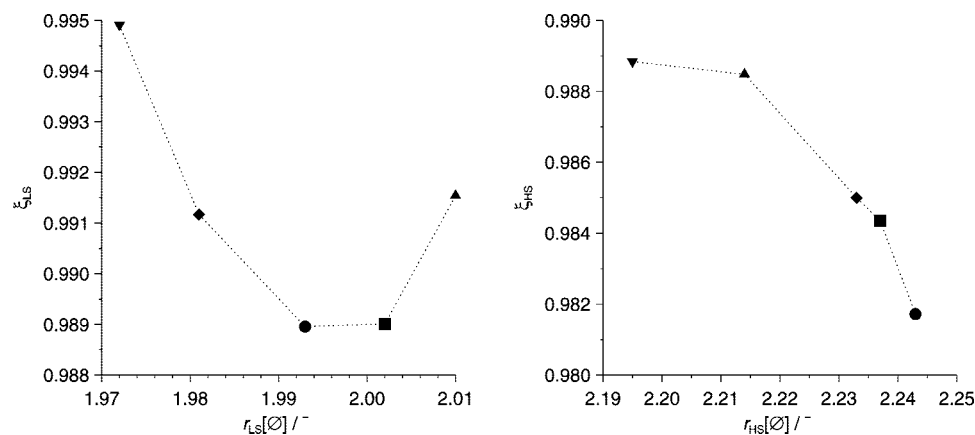
Figure 9. Plots of ξ_{LS} against $r_{LS}[\varnothing]$ (left) and of ξ_{HS} against $r_{HS}[\varnothing]$ (right) for the different XC functionals used: PBE/$\mathscr{G}$ (▼), B3LYP*/$\mathscr{G}$ (◆), HCTH/$\mathscr{G}$ (◆), O3LYP/$\mathscr{G}$ (■), and OLYP/$\mathscr{G}$ (●) results (lines serve to highlight the trends among the functionals).

Figure 10. Plots of $r_{LS}[Y]$ against $r_{LS}[\varnothing]$ (left) and of $r_{HS}[Y]$ against $r_{HS}[\varnothing]$ (right) for the different XC functionals used: PBE/$\mathscr{G}$ (▼), B3LYP*/$\mathscr{G}$ (▼), HCTH/$\mathscr{G}$ (◆), O3LYP/$\mathscr{G}$ (■) and OLYP/$\mathscr{G}$ (●) results (lines serve to highlight the trends among the functionals).

It thus follows that $E_{\Gamma}^{dist}\{Fe\}$ increases with the predicted degree of shrinking and distortion of the Γ geometry of [Fe(bpy)$_3$]$^{2+}$ as measured by ξ_{Γ} (Γ = LS, HS).

Can the above correlation between the calculated values of $E_{\Gamma}^{dist}\{Fe\}$ and ξ_{Γ} (Γ = LS, HS) be related to a particular tendency among the functionals? As shown in Figure 9, ξ_{HS} turns out to be a decreasing function of $r_{HS}[\varnothing]$. Note also in Figure 10 that $r_{\Gamma}[Y]$ is an increasing function of $r_{\Gamma}[\varnothing]$ (Γ = LS, HS). For the complex in the HS state, we therefore

observe the following trend among the functionals: the calculated $E_{HS}^{dist}\{Fe\}$ value is larger, the longer the predicted iron−nitrogen bond in the HS state. However, this trend is not observed for the complex in the LS state since ξ_{LS} does not vary monotonously with $r_{LS}[\varnothing]$ (Figure 9). Consequently, the influence of the choice of the XC functional on the calculated values of $E_{\Gamma}^{dist}\{Fe\}$ and ξ_{Γ} cannot be explained only by the tendency of the functionals to give more or less long metal−nitrogen bonds for [Fe(bpy)$_3$]$^{2+}$ in either spin state.

Actually, $E_\Gamma^{dist}\{Fe\}$ and ξ_Γ (Γ = HS, LS) are related not only to the extent of the structural changes which the complex in the Γ state must undergo to fit best into the supercage but also to the ability of the supercage to more or less readily host the complex in this spin state. This follows from the fact that the guest−host interactions in $[Fe(bpy)_3]^{2+}@Y$, at the origin of the structural changes experienced by the supercage and the complex, depend on the match between the void volume of the supercage and the volume of the complex, for which the metal−ligand distance provides an immediate measure. In addition, besides its influence on the description of the complex, the choice of the functional obviously also affects the description of the supercage and that of the guest−host interactions in $[Fe(bpy)_3]^{2+}@Y$. Therefore, the correlated variations in the predicted values of $E_\Gamma^{dist}\{Fe\}$ and ξ_Γ reflect the subtle interplay between the influence of the functionals on the description of the supercage, hence of its void volume, and their influence on the description of $[Fe(bpy)_3]^{2+}$ in the Γ state, hence of its volume.

We noticed that the correlation between $E_{HS}^{dist}\{Fe\}$ and ξ_{HS} also translates into a correlation between $E_{HS}^{dist}\{Fe\}$ and $r_{HS}[\varnothing]$. Such an observation implies that, in the HS state, the variations introduced by the use of the different functionals in the description of $[Fe(bpy)_3]^{2+}$ prevail over the manner in which these functionals influence the description of the supercage. The most plausible explanation is that the volume of the HS complex is so large that, with its encapsulation, the maximum capacity of the supercage regarding the inclusion of a tris(2,2′-bipyridine) complex is reached. This is nicely illustrated by the plot in Figure 10 of the predicted values of $r_{HS}[Y]$ against those of $r_{HS}[\varnothing]$. This tendency curve indeed has a negative curvature and presents at large $r_{HS}[\varnothing]$ values a plateau which suggests for $r_{HS}[Y]$ an upper limit of $\sim$2.202 Å. Note in passing the contrasting positive curvature of the tendency curve obtained for the LS complex of lesser volume by plotting the calculated values of $r_{LS}[Y]$ against those of $r_{LS}[\varnothing]$. We thus understand that the shrinkage and the distortion undergone by the structure of the HS complex are all the more pronounced ($\xi_{HS}\downarrow$) and destabilizing ($E_{HS}^{dist}\{Fe\}\uparrow$) that, first and foremost, the predicted gas-phase structure is expanded ($r_{HS}[\varnothing]\uparrow$).

The values predicted for $\Delta(\Delta E_{HL}^{el})$ with the various GGA and hybrid approximations to the universal XC functional average to 2445 cm^{-1} and present a standard deviation of 435 cm^{-1}. As this will be emphasized later on in the analysis of the guest−host interactions in $[Fe(bpy)_3]^{2+}@Y$, the physics of the embedding of $[Fe(bpy)_3]^{2+}$ in zeolite Y in either spin-state is quantitatively captured by the approximate functionals. We therefore propose as a fair estimate of $\Delta(\Delta E_{HL}^{el})$

$$\Delta(\Delta E_{HL}^{el}) = 2500 \pm 1000 \text{ cm}^{-1} \qquad (7)$$

3.3.2. Analysis of the Guest−Host Interactions in $[Fe(bpy)_3]^{2+}@Y$*.* To get insight into the physics of the involved guest−host interactions, we analyzed them using the bonding energy decomposition scheme implemented in the ADF package.[53,77] This decomposition scheme is similar to the energy decomposition analysis proposed by Morokuma

within the Hartree−Fock approximation,[78−80] and closely follows the one introduced within DFT by Ziegler and Rauk using the extended transition state method.[81−83] It has been successfully applied to the analysis of different bonding situations, as recently reviewed by Bickelhaupt and Baerends,[77] and by Frenking and co-workers.[84,85] Before giving our results, we briefly present the physically meaningful contributions to bonding interaction energies that are obtained with this partitioning scheme and refer the reader to the above reviews for detailed discussions of these contributions.

The bond dissociation energy between two fragments A and B, in our case, $[Fe(bpy)_3]^{2+}$ and the supercage, is divided into two major contributions E^{prep} and E^{int}. E^{prep} is the energy necessary to promote the fragments from their equilibrium geometry and electronic ground-state to their geometry and electronic state in the interacting system AB. Note that, for $[Fe(bpy)_3]^{2+}@Y$, we have already discussed the geometric contributions $E_\Gamma^{dist}\{Fe\}$ and $E_\Gamma^{dist}\{Y\}$ to E^{prep} (Γ = LS, HS). As for the electronic contribution to E^{prep}, we are in principle concerned with its determination only when dealing with $[Fe(bpy)_3]^{2+}@Y$ in the HS state. E^{int} is the instantaneous interaction energy between the prepared fragments. It can be broken down into three main components

$$E^{int} = E^{elstat} + E^{Pauli} + E^{orb} \qquad (8)$$

E^{elstat} corresponds to the classical electrostatic interaction between the unperturbed charge distributions of the prepared fragments, the overall density being the simple superposition of the fragment densities. E^{Pauli} corresponds to the Pauli repulsion, which is responsible for any steric repulsion between the fragments. It is the energy change that arises upon going from the simple superposition of the fragment densities to the wave function that obeys the Pauli principle through the antisymmetrization and normalization of the product of the fragment wave functions. Last, E^{orb} is the orbital interaction energy, that is, the energy gained by allowing the electron density to fully relax. It potentially includes the contributions from all conceivable stabilizing orbital interactions (electron pair bonding, charge transfer, polarization) and can be further decomposed into the contributions from the irreducible representations of the interacting system. Given that the calculations with ADF cannot be done using the C_3 symmetry of the $[Fe(bpy)_3]^{2+}@Y$ model, the partitioning of E^{orb} into the contributions from the e and a representations is not accessible.

The corresponding ADF calculations are single-point calculations performed at the OLYP/$\mathscr{S}$ level on optimized OLYP/$\mathscr{G}$ geometries. The $\mathscr{G} \rightarrow \mathscr{S}$ change of basis sets does not influence the description of the spin-states energetics. Indeed, the HS−LS energy differences obtained with these single-point calculations are $\Delta E_{HL}^{el}[\varnothing]$ = 3049 cm^{-1} and $\Delta E_{HL}^{el}[Y]$ = 5836 cm^{-1}, leading to $\Delta(\Delta E_{HL}^{el})$ = 2787 cm^{-1}, in excellent agreement with the OLYP/$\mathscr{G}$ results of Table 5. Note that the calculations targeted at the characterization of the HS state converged toward its ^5E component.

For $[Fe(bpy)_3]^{2+}@Y$ taken in a given geometry, the guest−host interactions are not affected by the electronic rearrangements within the metallic d orbitals. This can be

Table 6. Analysis of the Guest−Host Interactions in [Fe(bpy)$_3$]$^{2+}$@Y in the LS and HS States: Results of Calculations Performed at the OLYP/$\mathcal{I}$ Level Using the OLYP/$\mathcal{G}$ Optimized LS and HS Geometries (cm^{-1})

	E_Γ^{elstat}	E_Γ^{Pauli}	E_Γ^{orb}	E_Γ^{int}
Γ = LS	−15558	+17442	−12158	−10275
Γ = HS	−15251	+18099	−11874	−9026
	ΔE_{HL}^{elstat}	ΔE_{HL}^{Pauli}	ΔE_{HL}^{orb}	ΔE_{HL}^{int}
	+307	+657	+284	+1249

concluded from the energies of LS ↔ HS vertical transitions in [Fe(bpy)$_3$]$^{2+}$@Y, which can be calculated by considering either the whole system or the [Fe(bpy)$_3$]$^{2+}$ subsystem only. Thus, at the OLYP/$\mathcal{G}$ optimized LS geometry of [Fe(bpy)$_3$]$^{2+}$@Y, the OLYP/$\mathcal{I}$ values found for the energy of the LS → HS Franck−Condon excitation are 18 296 and 17 956 cm^{-1}, when the calculations are performed on the entire system and on the complex, respectively. Similarly, at the HS geometry of [Fe(bpy)$_3$]$^{2+}$@Y, the calculated energies of the LS ← HS Franck−Condon excitation are 4375 and 4397 cm^{-1}, respectively. The fact that the guest−host interactions at a fixed geometry of [Fe(bpy)$_3$]$^{2+}$@Y do not depend on the ligand-field state of [Fe(bpy)$_3$]$^{2+}$@Y originates from the strongly local character of vertical d−d excitations. Given this insensitivity of the guest−host interactions to the nature of the ligand-field state of the complex, we can identify them as closed-shell interactions between the first coordination sphere provided by the bipyridine ligands and the second coordination sphere defined by the supercage under the polarizing effects of the iron dication.

The fact that such interactions are accurately described by most modern XC functionals is the reason as to why there is a remarkably good consistency between the results obtained with the various functionals for the influence of encapsulation on the structural, energetic ($\Delta(\Delta E_{HL}^{el})$) and Mössbauer spectroscopy properties of [Fe(bpy)$_3$]$^{2+}$. The guest−host interactions at any given geometry of [Fe(bpy)$_3$]$^{2+}$@Y can simply be characterized in the LS manifold. We proceeded this way for analyzing the guest−host interactions at the LS as well as at the HS geometry of [Fe(bpy)$_3$]$^{2+}$@Y. Table 6 summarizes the results. In either spin-state, the attractive components of the interaction energy, E_Γ^{elstat} and E_Γ^{orb}, are smaller in magnitude than the Pauli repulsion E_Γ^{Pauli}, but together they do more than compensate this latter, thus leading to overall stabilizing guest−host interactions $E_\Gamma^{int} < 0$ (Γ = LS, HS). One also notes that E_Γ^{elstat} is larger in magnitude than E_Γ^{orb}: that is, the bonding between the complex and the supercage in the two spin-states is more electrostatic than covalent. Upon the LS → HS change of spin-states, the guest−host interactions become less stabilizing, with a predicted increase of ΔE_{HL}^{int} = +1249 cm^{-1}, which is in very good agreement with the previously determined ΔE_{HL}^{int} values (Table 5).

As a consequence of the expansion of the complex upon the LS → HS transition, the Pauli repulsion increases. This interaction corresponds to four-electron two-orbital destabilizing interactions, which are all the more destabilizing the

larger the orbital overlap. The expansion of [Fe(bpy)$_3$]$^{2+}$ indeed brings the ligands and the supercage closer to each other, thus increasing the overlap between the molecular orbitals (MOs) of the supercage and those of the complex. However, the increase of the Pauli repulsion accounts only for ∼53% of ΔE_{HL}^{int}. The electrostatic and orbital interactions both become also less attractive, and the corresponding energy increases account for ∼25% and ∼22% of ΔE_{HL}^{int}, respectively. The increase of the electrostatic interaction shows that the electronic and nuclear repulsions between the two subsystems increase with respect to the attractive interactions between the electronic charge distribution of one subsystem with the nuclei of the other. In passing from the LS to the HS state, the distortions experienced by the complex and, to a far lesser extent, by the supercage are accompanied by changes in the energies and shapes of their MOs. These changes, combined with the unavailability of the decomposition of the orbital interaction into the contributions from the representations a and e, prevent determination of the reasons as to the observed variation of the orbital interaction.

Noticing the insensivity of the guest−host interactions to the spin-state of [Fe(bpy)$_3$]$^{2+}$, we substituted the Fe^{2+} ion with the 4d^6 Ru^{2+} and 3d^{10} Zn^{2+} ions to assess the influence of the nature of the transition metal dication on these interactions.[86] Thus, using the OLYP/$\mathcal{G}$ optimized geometry of LS [Fe(bpy)$_3$]$^{2+}$@Y, the analysis of the guest−host interactions in the Fe^{2+} → Zn^{2+} substituted [Zn(bpy)$_3$]$^{2+}$@Y system at the OLYP/$\mathcal{I}$ level gives E_{LS}^{int} = −10 287 cm^{-1} with E_{LS}^{elstat} = −15 569 cm^{-1}, E_{LS}^{Pauli} = 17 697 cm^{-1}, and E_{LS}^{orb} = −12 415 cm^{-1}. For the Fe^{2+} → Ru^{2+} substituted LS [Ru(bpy)$_3$]$^{2+}$@Y system, we similarly obtain E_{LS}^{int} = −10 282 cm^{-1} with E_{LS}^{elstat} = −15 613 cm^{-1}, E_{LS}^{Pauli} = 17 853 cm^{-1}, and E_{LS}^{orb} = −12 523 cm^{-1}. For either substituted [M(bpy)$_3$]$^{2+}$@Y system (M = Fe, Zn), the value of the bonding energy between the [M(bpy)$_3$]$^{2+}$ complex and the supercage and those of its three components perfectly match those obtained from the analysis of the guest−host interactions in the original LS [Fe(bpy)$_3$]$^{2+}$@Y system (Table 6). This shows that, for a given geometry of a transition metal system [M(bpy)$_3$]$^{2+}$@Y, the interactions between the [M(bpy)$_3$]$^{2+}$ complex and the supercage depend neither on the spin state of the transition metal dication M^{2+} nor on its nature.

Finally, the whole destabilization $\Delta(\Delta E_{HL}^{el})$ of the HS state with regard to the LS state upon encapsulation can be viewed as resulting from the need to keep the decrease ΔE_{HL}^{int} of the stabilizing guest−host interactions minimal, at the expense ΔE_{HL}^{dist} of increased distortions of the two moieties of [Fe(bpy)$_3$]$^{2+}$@Y upon the LS → HS transition. The distortions undergone by the complex give the dominant contribution to ΔE_{HL}^{dist} (Table 5). In this respect, let us point out the fact that, in both spin states, but especially in the HS state, the encapsulation of [Fe(bpy)$_3$]$^{2+}$ is accompanied by large deformations along the γ angular coordinate (Tables 1 and 3), which actually are associated with floppy modes.[6] Hence, while the sizable increase of the molecular volume of [Fe(bpy)$_3$]$^{2+}$ entailed by the LS → HS change of spin-states is at the origin of the influence of the encapsulation on the spin-state energetics, the ability of the complex to thus readily

distort along such floppy modes helps moderate this desta-bilizing influence.

3.3.3. HS−LS Energy Difference and the Low-Temperarure Dynamics of the HS → LS Relaxation in [Fe(bpy)₃]²⁺@Y. Pierloot and Vancoillie recently dem-onstrated the feasability of high-level wave function-based calculations with the CASPT2 method and extensive basis sets for the determination of the HS−LS electronic energy difference in the isolated [Fe(bpy)₃]²⁺ complex, as well as in other iron(II) complexes of similar size.[69,75] Their studies, based on single-point CASPT2 calculations on DFT-optimized LS and HS geometries, led, for the gas-phase value of ΔE_{HL}^{el} in [Fe(bpy)₃]²⁺, to the currently most accurate ab initio estimate of[69,75]

$$\Delta E_{HL}^{el}[\varnothing] = 3700 \pm 1000 \text{ cm}^{-1} \qquad (9)$$

Using eq 3 and the independent estimates of $\Delta(\Delta E_{HL}^{el})$ and $\Delta E_{HL}^{el}[\varnothing]$, we obtain for the value of ΔE_{HL}^{el} in the zeolite-Y encapsulated complex a best ab initio estimate of

$$\Delta E_{HL}^{el}[Y] = 6200 \pm 1500 \text{ cm}^{-1} \qquad (10)$$

The comparison of the calculated $\Delta E_{HL}^{el}[Y]$ values given in Table 5A with the above estimate shows that there is a remarkably good agreement for the results obtained with the OLYP and B3LYP* functionals. This follows from the fact (i) that these two functionals perform well for the determi-nation of $\Delta E_{HL}^{el}[\varnothing]$ in [Fe(bpy)₃]²⁺, as also previously reported,[6,67,69,75] and (ii) that the different functionals give $\Delta(\Delta E_{HL}^{el})$ values that are very consistent with one another.

The low-temperature dynamics of the HS → LS relaxation in the [Fe(bpy)₃]²⁺@Y compound are determined by the HS−LS zero-point energy difference $\Delta E_{HL}^{\circ}[Y]$. This one divides into an electronic contribution, $\Delta E_{HL}^{el}[Y]$, whose predicted value is given above, and a vibrational contribution, $\Delta E_{HL}^{vib}[Y]$. Within our approach to the theoretical study of [Fe(bpy)₃]²⁺@Y, the determination of this latter contribution rigorously requires that a vibrational analysis be performed for the whole model system in the LS and in the HS state. However, given that the supercage is hardly affected by the structural changes undergone by the complex upon the LS → HS change of spin states, this computationally demanding task is avoided by considering the supercage as being rigid and, afterward, by taking $\Delta E_{HL}^{vib}[Y]$ as being caused by the shifts in the vibrational frequencies centered on the encap-sulated complex upon the LS → HS change of spin-states. Because of the weakening of the metal−ligand bond in passing from the LS to the HS state, $\Delta E_{HL}^{vib}[Y]$ is negative. Furthermore, the structure of the encapsulated complex in either spin-state remaining close to that of the isolated complex in the same spin manifold, it is reasonable to assume that $\Delta E_{HL}^{vib}[Y]$ is comparable in magnitude to $\Delta E_{HL}^{vib}[\varnothing]$, the vibrational contribution to the HS−LS zero-point energy difference of the isolated complex. A value of $\Delta E_{HL}^{vib}[\varnothing] = -875$ cm⁻¹ was previously reported.[6] Actually, $|\Delta E_{HL}^{vib}[Y]|$ is probably slightly smaller than $|\Delta E_{HL}^{vib}[\varnothing]|$ because the shrinkage of the structure of the complex entailed by the encapsulation is larger in the HS state than in the LS state. We therefore propose for $\Delta E_{HL}^{vib}[Y]$ a model value of

$\Delta E_{HL}^{vib}[Y] = -800$ cm⁻¹. This gives for ΔE_{HL}° in [Fe(bpy)₃]²⁺@Y a best estimate of

$$\Delta E_{HL}^{\circ}[Y] = 5400 \pm 1500 \text{ cm}^{-1} \qquad (11)$$

On the basis of the HS → LS relaxation theory,[7] we could deduce from this $\Delta E_{HL}^{\circ}[Y]$ value that the lifetime $\tau_{HS}[Y]$ of the metastable HS state in [Fe(bpy)₃]²⁺@Y is below 10 ns.

4. Concluding Remarks

The application of DFT to the study of the guest−host interactions in [Fe(bpy)₃]²⁺@Y within a supramolecular approach allowed us to gain major new insights into the nature of these interactions and into their influence on the structural, energetic and Mössbauer spectroscopy properties of the complex in the LS and HS states. The main results and conclusions are summarized below.

(1) Guest−Host Interactions. The guest−host interactions at a given geometry of [Fe(bpy)₃]²⁺@Y do not depend on the spin state of the complex. We ascribed this to the fact that the vertical d−d excitations involved in a change of ligand-field states have a strongly local character. By substituting Fe²⁺ with Ru²⁺ and Zn²⁺, we also showed that varying the nature of the transition metal dication does not affect the guest−host interactions. These interactions are closed-shell inter-actions between the first coordination sphere provided by the 2,2′-bipyridine ligands and the second coordi-nation sphere defined by the supercage under the polarizing effects of the transition metal dication. They are accurately described by most modern functionals, and in this respect, the different GGA (PBE, HCTH, OLYP) and hybrid (B3LYP*, O3LYP) functionals used very consistently predict an increase in the interaction energy of $\Delta E_{HL}^{int} \approx 1300$ cm⁻¹ upon the LS → HS transition.

The analysis of the guest−host interaction energy at the LS and HS geometries of[5] [Fe(bpy)₃]²⁺@Y showed that these interactions are stabilizing and that the resulting bonding is more electrostatic than covalent. In passing from the LS to the HS state, there is an increase of the Pauli or steric repulsion, which is expected from the expansion of the complex upon this change of spin states. The Pauli repulsion however contributes only to about half of ΔE_{HL}^{int}. The electro-static and orbital interactions also become less stabi-lizing and their increases contribute almost equally to the remaining part of ΔE_{HL}^{int}.

(2) Structural Properties. Our results show that, upon encapsulation, the structure of the complex shrinks and distorts to an extent which increases in passing from the LS to the HS state. The supercage also undergoes geometric changes so as to host the [Fe(bpy)₃]²⁺ complex, but its structure turns out to hardly evolve upon the LS → HS change of spin-states and the concomitant expansion of its guest. A relevant measure of the structural changes experienced by the complex proves to be the ratio $\xi_{\Gamma} = r_{\Gamma}[Y]/r_{\Gamma}[\varnothing]$, where r_{Γ} is the average iron−nitrogen bond length in the Γ state (Γ = LS, HS). The smaller the ratio, the more

pronounced the structural changes. Because of the approximate nature of the functionals used, the calculated geometries exhibit small but noticeable differences, and varying degrees of distortion and shrinkage are observed. In either spin state, these last ones are found to increase with the functionals in the order PBE < B3LYP* < HCTH < O3LYP < OLYP. Still, the shrinkage and distortion experienced by the complex in either spin state are not such that this translates into a sizable variation of the quadrupole splitting ΔE_Q at the iron center.

(3) ^{57}Fe Quadrupole Splitting. The values of ΔE_Q in LS and HS [Fe(bpy)$_3$]$^{2+}$ and [Fe(bpy)$_3$]$^{2+}$@Y were obtained from the results of relativistic EFG calculations performed at the OLYP level within the ZORA and ZORA-4 approximations on the different optimized geometries. The two relativistic approximations give very similar results and the remarkable consistency observed among the results of EFG calculations performed with the OLYP and PBE functionals suggests that the choice of the XC functional has a negligible influence on the results.[87] For [Fe(bpy)$_3$]$^{2+}$@Y, ΔE_Q could accurately be calculated by considering the [Fe(bpy)$_3$]$^{2+}$ subsystem only. The contribution of the outer coordination sphere to the EFG at the iron center was indeed shown to be vanishing. The main trend observed in both spin-states is that, as a consequence of the shrinking and distortion undergone by the complex, the quadrupole splitting increases in passing from the isolated complex of D_3 symmetry to the encapsulated complex of C_3 symmetry: $\Delta E_Q[\varnothing] < \Delta E_Q[Y]$.

The increase of ΔE_Q upon encapsulation depends on the predicted degree of shrinking and distortion experienced by the complex. In the LS state, $\Delta E_Q[\varnothing] \cong -0.38$ mm s^{-1} and $\Delta E_Q[Y]$ varies between -0.37 and -0.32 mm s^{-1} depending on the functional used in the optimization calculations. In the HS state, we have $\Delta E_Q[\varnothing] \cong 1.33$ mm s^{-1} and $\Delta E_Q[\varnothing] \cong -2.68$ mm s^{-1} for [Fe(bpy)$_3$]$^{2+}$ in the ^5E and ^5A HS states, respectively. For HS [Fe(bpy)$_3$]$^{2+}$@Y, the EFG could be calculated for the ^5E state only, and this gives $\Delta E_Q[Y]$ values of between 1.37 and 1.40 mm s^{-1} depending on the considered HS geometry. For the complex in the ^5A state, we expect similar increases of the quadrupole splitting upon encapsulation. Deisenroth et al. determined for the HS complex in the [Co(bpy)$_3$](PF$_6$)$_2$ matrix $|\Delta E_Q| = 1.17$ mm s^{-1}.[3] The good agreement between this value and those determined for the complex in the ^5E state shows that this state is the lowest-lying component of the HS state for [Fe(bpy)$_3$]$^{2+}$ doped into [Co(bpy)$_3$](PF$_6$)$_2$. The molecular volume of [Fe(bpy)$_3$]$^{2+}$ is slightly larger in the ^5A state than in the ^5E state and the two HS states are nearly degenerate in the isolated complex.[6] Consequently, the energy ordering observed for the two components of the HS state in the [Co(bpy)$_3$](PF$_6$)$_2$ matrix can be ascribed to the chemical pressure exerted by the environment, which destabilizes the ^5A state

with respect to the ^5E state. Given the confining environment provided by the supercage of zeolite Y, we expect this same energy ordering in [Fe(bpy)$_3$]$^{2+}$@Y.

(4) Spin-State Energetics. The XC functionals used perform very differently for the determination of the HS−LS energy difference ΔE_{HL}^{el} in both [Fe(bpy)$_3$]$^{2+}$ and [Fe(bpy)$_3$]$^{2+}$@Y. However, thanks to their converging performances for the accurate description of the guest−host interactions in [Fe(bpy)$_3$]$^{2+}$@Y, they perform very similarly for predicting the change of this energy difference upon encapsulation: $\Delta(\Delta E_{HL}^{el}) = +2500 \pm 1000$ cm^{-1}.

Of the two components ΔE_{HL}^{int} and ΔE_{HL}^{dist} of $\Delta(\Delta E_{HL}^{el})$, the latter is the one responsible for the uncertainty in the determination of $\Delta(\Delta E_{HL}^{el})$. While $\Delta E_{HL}^{int} \approx 1300$ cm^{-1} at all levels, the calculated values of the geometric contribution ΔE_{HL}^{dist} noticeably depend on the functionals used (Table 5). $\Delta E_{HL}^{dist} = E_{HS}^{dist} - E_{LS}^{dist}$, where E_{Γ}^{dist} is the energy needed to bring the Γ complex and the supercage from their gas-phase geometries to their geometries in Γ [Fe(bpy)$_3$]$^{2+}$@Y (Γ = LS, HS). The calculated E_{Γ}^{dist} values increase with the degree of shrinkage and distortion predicted for the complex in a given spin state. Their dispersion reflects the varying errors made with the different functionals in describing both subsytems at and in the vicinity of the minima of their potential energy surfaces. The propagation of this dispersion to the calculated ΔE_{HL}^{dist} values shows that the errors made in determining E_{LS}^{dist} and E_{HS}^{dist} with a given functional tend to only partly compensate when it comes to evaluate ΔE_{HL}^{dist}. This implies that improving the accuracy in the determination of $\Delta(\Delta E_{HL}^{el})$ requires the use of functionals which accurately describe the geometries of transition metal complexes in different spin-states. Note that the $\Delta(\Delta E_{HL}^{el})$ values obtained with the very various functionals used actually average to 2445 cm^{-1} with a standard deviation of $\sigma = 435$ cm^{-1}. Consequently, improving the accuracy of the description of the geometries of [Fe(bpy)$_3$]$^{2+}$ in both spin states should not lead to a significant change in the $\Delta(\Delta E_{HL}^{el})$ best estimate of 2500 cm^{-1}, but rather mainly help reduce the uncertainty of ± 1000 cm^{-1} (i.e., $\sim 2\sigma$) put on this value.

Finally, from our calculated $\Delta(\Delta E_{HL}^{el})$ value and the CASPT2 estimate of ΔE_{HL}^{el} in the isolated complex,[69,75] $\Delta E_{HL}^{el}[\varnothing] = 3700 \pm 1000$ cm^{-1}, we could obtain for ΔE_{HL}^{el} in [Fe(bpy)$_3$]$^{2+}$@Y a best ab initio estimate of $\Delta E_{HL}^{el}[Y] = 6200 \pm 1500$ cm^{-1}. Our supramolecular approach to the study of the guest−host interactions in [Fe(bpy)$_3$]$^{2+}$@Y and their influence on the physicochemical properties of [Fe(bpy)$_3$]$^{2+}$ allowed us to quantitatively capture the whole picture. The conclusions thus drawn regarding the influence of the confining environment provided by the supercage on the relative energies of the ligand-field states of [Fe(bpy)$_3$]$^{2+}$ readily extend to other [M(bpy)$_3$]$^{2+}$@Y systems. This immediately follows from the insensi-

Properties of Iron(II)tris(2,2′-bipyridine)

J. Chem. Theory Comput., Vol. 5, No. 1, 2009 **113**

tivity of the guest−host interactions, at a given geometry of $[M(bpy)_3]^{2+}@Y$, to the nature of the transition metal cation. So, upon the encagement of a d^n $[M(bpy)_3]^{2+}$ complex, a ligand-field state originating from a $t_{2g}^{n-p-1}e_g^{p+1}$ configuration will be destabilized with regard to a ligand-field state originating from the $t_{2g}^{n-p}e_g^p$ $(p \leq n-1)$. Indeed, the equilibrium geometry of the complex is more expanded in the former state than in the latter. However, given that the equilibrium geometries of the complex in these states depend on the nature of the transition metal, the variations of the relative energies of the ligand-field states can only be determined through dedicated studies. Our supramolecular approach is thus being applied to the study of $[Co(bpy)_3]^{2+}@Y$ to determine how the guest−host interactions turn the intermediate-field $[Co(bpy)_3]^{2+}$ complex with usually a HS ground-state into a spin-crossover system.

This approach can be applied to the study of the physico-chemical properties of zeolite-Y encapsulated complexes other than tris(2,2′-bipyridine) complexes. For instance, it would help rationalize the observation made by Maruszewski et al. that the encapsulation entails an increase in energy of the excited d−d quencher state in $[Ru(bpy)_3]^{2+}$ but also in other Ru(II) polypyridine complexes of similar size.[90] But, more generally, it can be used to address the prediction of the influence of the environments provided by different hosting cavities on the physicochemical properties of a given complex. In this respect, zeolites provide cavities of very various sizes and shapes.[91,92] Metal−organic frameworks (MOFs) are also appealing porous materials,[93−96] Alkordi et al. having recently reported the encagement of metal-loporphyrins into a zeolite-like MOF.[97] Hence, there is a wide applicability of the supramolecular approach used for investigating $[Fe(bpy)_3]^{2+}@Y$, which makes it quite promising for exploring and tailoring the properties of inclusion compounds of transition metal complexes.

Supporting Information Available: Influence of the starting geometry on the outcome of the geometry optimization of $[Fe(bpy)_3]^{2+}@Y$, influence of the choice of the functional on the calculation of the quadrupole splitting, LS and HS geometries of $[Fe(bpy)_3]^{2+}@Y$ calculated at the OLYP/$\mathscr{G}$ level and scripts which allow their visualization using the Jmol program. This material is available free of charge via the Internet at http://pubs.acs.org.

References

(1) Hauser, A. *Top. Curr. Chem.* **2004**, *234*, 155–198.

(2) Hauser, A. *Chem. Phys. Lett.* **1990**, *173*, 507–512.

(3) Deisenroth, S.; Hauser, A.; Spiering, H.; Gütlich, P. *Hyperfine Interact.* **1994**, *93*, 1573–1577.

(4) Schenker, S.; Hauser, A.; Wang, W.; Chan, I. Y. *Chem. Phys. Lett.* **1998**, *297*, 281–286.

(5) Hauser, A.; Amstutz, N.; Delahaye, S.; Sadki, A.; Schenker, S.; Sieber, R.; Zerara, M. *Struct. Bonding (Berlin)* **2004**, *106*, 81–96.

(6) Lawson Daku, L. M.; Vargas, A.; Hauser, A.; Fouqueau, A.; Casida, M. E. *ChemPhysChem* **2005**, *6*, 1393–1410.

(7) Hauser, A.; Enachescu, C.; Lawson Daku, M.; Vargas, A.; Amstutz, N. *Coord. Chem. Rev.* **2006**, *250*, 1642–1652.

(8) Gawelda, W.; Pham, V.-T.; Benfatto, M.; Zaushitsyn, Y.; Kaiser, M.; Grolimund, D.; Johnson, S. L.; Abela, R.; Hauser, A.; Bressler, C.; Chergui, M. *Phys. Rev. Lett.* **2007**, *98*, 057401.

(9) Nishikiori, S.; Yoshikawa, H.; Sano, Y.; Iwamoto, T. *Acc. Chem. Res.* **2005**, *38*, 227–234.

(10) Sugi, M.; Matsumoto, Y.; Kimura, N.; Komatsubara, T.; Aoki, H.; Terashima, T.; Uji, S. *Phys. Rev. Lett.* **2008**, *101*, 056401.

(11) Espallargas, G. M.; Brammer, L.; Allan, D. R.; Pulham, C. R.; Robertson, N.; Warren, J. E. *J. Am. Chem. Soc.* **2008**, *130*, 9058–9071.

(12) Sampathkumaran, E. V.; Dhar, S. K.; Malik, S. K. *J. Phys. C: Solid State Phys.* **1987**, *20*, L53–L56.

(13) Lawson Daku, L. M.; Hagemann, H. *Phys. Rev. B* **2007**, *76*, 014118.

(14) Gol'tsov, Y. G. *Theor. Exp. Chem.* **1999**, *35*, 183–197.

(15) Payra, P.; Dutta, P. K. In *Handbook of Zeolite Science and Technology*; Auerbach, S. M., Carrado, K. A., Dutta, P. K., Eds.; Marcel Dekker Publishing: New York, 2003, pp 1−19.

(16) DeWilde, W.; Peeters, G.; Lunsford, J. H. *J. Phys. Chem.* **1980**, *84*, 2306–2310.

(17) Herron, N. *Inorg. Chem.* **1986**, *25*, 4714–4717.

(18) Quayle, W. H.; Peeters, G.; De Roy, G. L.; Vansant, E. F.; Lunsford, J. H. *Inorg. Chem.* **1982**, *21*, 2226–2231.

(19) Umemura, Y.; Minai, Y.; Tominaga, T. *J. Chem. Soc., Chem. Commun.* **1993**, 1822–1823.

(20) Vankó, G.; Homonnay, Z.; Nagy, S.; Vértes, A.; Pál-Borbély, G.; Beyer, H. K. *Chem. Commun.* **1996**, 785–786.

(21) Umemura, Y.; Minai, Y.; Tominaga, T. *J. Phys. Chem. B* **1999**, *103*, 647–652.

(22) Vijayalakshmi, R.; Kulshreshtha, S. K. *Microporous Mesoporous Mater.* **2008**, *111*, 449–454.

(23) Gütlich, P.; Hauser, A.; Spiering, H. *Angew. Chem., Int. Ed. Engl.* **1994**, *33*, 2024–2054.

(24) Zhang, Y.; Oldfield, E. *J. Phys. Chem. A* **2003**, *107*, 4147–4150.

(25) Gütlich, P.; Goodwin, H. A. *Top. Curr. Chem.* **2004**, *233*, 1–47.

(26) Paulsen, H.; Schünemann, V.; Trautwein, A. X.; Winkler, H. *Coord. Chem. Rev.* **2005**, *249*, 255–272.

(27) Remacle, F.; Grandjean, F.; Long, G. J. *Inorg. Chem.* **2008**, *47*, 4005–4014.

(28) Umemura et al.[19,21] predicted that the Mössbauer spectroscopic features of [Fe(bpy)$_3$]$^{2+}$@Y are $\delta = 0.5$ mm s^{-1} and $\Delta E_Q = 1.4-1.5$ mm s^{-1}. Recently, Vijayalakshmi and Kulshreshtha[22] also reported for the encapsulated complex, $\delta = 0.37$ mm s^{-1} and $\Delta E_Q = 0.81$ mm s^{-1}. These values of the quadrupole splitting are significantly larger than that of $\Delta E_Q \approx 0.3$ mm s^{-1} determined for [Fe(bpy)$_3$]$^{2+}$@Y by Quayle et al.[18] and by Vankó et al.[20] Hence, according to these results, one would draw the conclusion that the complex becomes strongly distorted in the zeolite Y. However, Vankó et al. demonstrated that such Mössbauer features cannot be assigned to [Fe(bpy)$_3$]$^{2+}$@Y but rather to uncomplexed iron cations located in the small cavities of the zeolite framework.[20] To this end, they blocked these cavities with La^{3+} ions before proceeding to the bottle-in-a-ship synthesis of [Fe(bpy)$_3$]$^{2+}$@Y. By proceeding so, they obtained [Fe(bpy)$_3$]$^{2+}$ as the unique included iron species, as attested for by the Mössbauer spectrum of the final compound which consists of a single quadrupole doublet with a narrow linewidth of 0.25 mm s^{-1} and with $\delta = 0.32$ mm s^{-1} and with $\Delta E_Q = 0.32$ mm s^{-1}.

(29) Hohenberg, P.; Kohn, W. *Phys. Rev.* **1964**, *136*, B864–B871.

(30) Kohn, W.; Sham, L. J. *Phys. Rev.* **1965**, *140*, A1133–A1138.

(31) Parr, R. G.; Yang, W. *Density-Functional Theory of Atoms and Molecules*; Oxford University Press: New York, 1989.

(32) Dreizler, R. M.; Gross, E. K. U. *Density Functional Theory, An Approach to the Quantum Many-Body Problem*; Springer-Verlag: New York, 1990.

(33) Koch, W.; Holthausen, M. C. *A Chemist's Guide to Density Functional Theory*; Wiley-VCH: New York, 2000.

(34) Homonnay, Z.; Vankó, G.; Vértes, A.; Nath, A.; Spiering, H.; Gütlich, P. *Hyperfine Interact.* **1998**, *113*, 331–339.

(35) Vankó, G.; Homonnay, Z.; Nagy, S.; Vértes, A.; Spiering, H.; Gütlich, P. *J. Chem. Phys.* **1998**, *108*, 8472–8478.

(36) Vankó, G.; Nagy, S.; Homonnay, Z.; Vértes, A. *Hyperfine Interact.* **2000**, *126*, 163–167.

(37) Deisenroth, S.; Spiering, H.; Nagy, D. L.; Gütlich, P. *Hyperfine Interact.* **1998**, *113*, 351–355.

(38) Frisch, M. J.; Trucks, G. W.; Schlegel, H. B.; Scuseria, G. E.; Robb, M. A.; Cheeseman, J. R.; Montgomery, J. A., Jr.; Vreven, T.; Kudin, K. N.; Burant, J. C.; Millam, J. M.; Iyengar, S. S.; Tomasi, J.; Barone, V.; Mennucci, B.; Cossi, M.; Scalmani, G.; Rega, N.; Petersson, G. A.; Nakatsuji, H.; Hada, M.; Ehara, M.; Toyota, K.; Fukuda, R.; Hasegawa, J.; Ishida, M.; Nakajima, T.; Honda, Y.; Kitao, O.; Nakai, H.; Klene, M.; Li, X.; Knox, J. E.; Hratchian, H. P.; Cross, J. B.; Bakken, V.; Adamo, C.; Jaramillo, J.; Gomperts, R.; Stratmann, R. E.; Yazyev, O.; Austin, A. J.; Cammi, R.; Pomelli, C.; Ochterski, J. W.; Ayala, P. Y.; Morokuma, K.; Voth, G. A.; Salvador, P.; Dannenberg, J. J.; Zakrzewski, V. G.; Dapprich, S.; Daniels, A. D.; Strain, M. C.; Farkas, O.; Malick, D. K.; Rabuck, A. D.; Raghavachari, K.; Foresman, J. B.; Ortiz, J. V.; Cui, Q.; Baboul, A. G.; Clifford, S.; Cioslowski, J.; Stefanov, B. B.; Liu, G.; Liashenko, A.; Piskorz, P.; Komaromi, I.; Martin, R. L.; Fox, D. J.; Keith, T.; Al-Laham, M. A.; Peng, C. Y.; Nanayakkara, A.; Challacombe, M.; Gill, P. M. W.; Johnson, B.; Chen, W.; Wong, M. W.; Gonzalez, C.; Pople, J. A. *Gaussian 03*, revision B.03/D.01; Gaussian, Inc.: Pittsburgh, PA, 2003.

(39) Lee, C.; Yang, W.; Parr, R. G. *Phys. Rev. B* **1988**, *37*, 785–789.

(40) Handy, N. C.; Cohen, A. J. *Mol. Phys.* **2001**, *99*, 403–412.

(41) Reiher, M.; Salomon, O.; Hess, B. A. *Theor. Chem. Acc.* **2001**, *107*, 48–55.

(42) Salomon, O.; Reiher, M.; Hess, B. A. *J. Chem. Phys.* **2002**, *117*, 4729–4737.

(43) Reiher, M. *Inorg. Chem.* **2002**, *41*, 6928–6935.

(44) Boese, A. D.; Handy, N. C. *J. Chem. Phys.* **2001**, *114*, 5497–5503.

(45) Cohen, A. J.; Handy, N. C. *Mol. Phys.* **2001**, *99*, 607–615.

(46) Perdew, J. P.; Burke, K.; Ernzerhof, M. *Phys. Rev. Lett.* **1996**, *77*, 3865–3868.

(47) Perdew, J. P.; Burke, K.; Ernzerhof, M. *Phys. Rev. Lett.* **1997**, *78*, 1396.

(48) Hehre, W. J.; Ditchfield, R.; Pople, J. A. *J. Chem. Phys.* **1972**, *56*, 2257–2261.

(49) Hariharan, P. C.; Pople, J. A. *Theor. Chim. Acta* **1973**, *28*, 213–222.

(50) Stevens, W. J.; Basch, H.; Krauss, M. *J. Chem. Phys.* **1984**, *81*, 6026–6033.

(51) Stevens, W. J.; Krauss, M.; Basch, H.; Jasien, P. G. *Can. J. Chem.* **1992**, *70*, 612–630.

(52) *Amsterdam Density Functional Program*, release ADF2004.01; Theoretical Chemistry, Vrije Universiteit: Amsterdam, The Netherlands, 2004; http://www.scm.com (accessed Nov 2, 2008).

(53) te Velde, G.; Bickelhaupt, F. M.; Baerends, E. J.; Fonseca Guerra, C.; van Gisbergen, S. J. A.; Snijders, J. G.; Ziegler, T. *J. Comput. Chem.* **2001**, *22*, 931–967.

(54) van Lenthe, E.; Baerends, E. J. *J. Chem. Phys.* **2000**, *122*, 8279–8292.

(55) Jmol: An open-source Java viewer for chemical structures in 3D. http://www.jmol.org (accessed Nov 2, 2008).

(56) McMahon, B.; Hanson, R. M. *J. Appl. Crystallogr.* **2008**, *41*, 811–814.

(57) Dick, S. *Z. Kristallogr.−New Cryst. Struct.* **1998**, *213*, 356.

(58) Schwerdtfeger, P.; Söhnel, T.; Pernpointner, M.; Laerdahl, J. K.; Wagner, F. E. *J. Chem. Phys.* **2001**, *115*, 5913–5924.

(59) *Principles and Applications of Density Functional Theory in Inorganic Chemistry I, II*; Kaltsoyannis, N., McGrady, J. E., Eds.; Springer-Verlag: Berlin, Germany, 2004.

(60) Paulsen, H.; Duelund, L.; Winkler, H.; Toftlund, H.; Trautwein, A. X. *Inorg. Chem.* **2001**, *40*, 2201–2204.

(61) Ghosh, A.; Taylor, P. R. *Curr. Opin. Chem. Biol.* **2003**, *7*, 113–124.

(62) Paulsen, H.; Trautwein, A. X. *Top. Curr. Chem.* **2004**, *235*, 197–219.

(63) Deeth, R. J.; Fey, N. *J. Comput. Chem.* **2004**, *25*, 1840–1848.

(64) Fouqueau, A.; Mer, S.; Casida, M. E.; Lawson Daku, L. M.; Hauser, A.; Mineva, T. *J. Chem. Phys.* **2004**, *120*, 9473–9486.

(65) Fouqueau, A.; Casida, M. E.; Lawson Daku, L. M.; Hauser, A.; Neese, F. *J. Chem. Phys.* **2005**, *122*, 044110.

(66) Smith, D. M. A.; Dupuis, M.; Straatsma, T. P. *Mol. Phys.* **2005**, *103*, 273–278.

(67) Ganzenmüller, G.; Berkaïne, N.; Fouqueau, A.; Casida, M. E. *J. Chem. Phys.* **2005**, *122*, 234321.

(68) Vargas, A.; Zerara, M.; Krausz, E.; Hauser, A.; Lawson Daku, L. M. *J. Chem. Theory Comput.* **2006**, *2*, 1342–1359.

(69) Pierloot, K.; Vancoillie, S. *J. Chem. Phys.* **2006**, *125*, 124303.

(70) Zein, S.; Borshch, S. A.; Fleurat-Lessard, P.; Casida, M. E.; Chermette, H. *J. Chem. Phys.* **2007**, *126*, 014105.

(71) Krivokapic, I.; Zerara, M.; Lawson Daku, M.; Vargas, A.; Enachescu, C.; Ambrus, C.; Tregenna-Piggott, P.; Amstutz, N.; Krausz, E.; Hauser, A. *Coord. Chem. Rev.* **2007**, *251*, 364–378.

(72) Conradie, J.; Ghosh, A. *J. Chem. Theory Comput.* **2007**, *3*, 689–702.

(73) Guillon, T.; Salmon, L.; Molnár, G.; Zein, S.; Borshch, S.; Bousseksou, A. *J. Phys. Chem. A* **2007**, *111*, 8223–8228.

(74) Scherlis, D. A.; Cococcioni, M.; Sit, P.; Marzari, N. *J. Phys. Chem. B* **2007**, *111*, 7384–7391.

(75) Pierloot, K.; Vancoillie, S. *J. Chem. Phys.* **2008**, *128*, 034104.

(76) Marti, K. H.; Ondík, I. M.; Moritz, G.; Reiher, M. *J. Chem. Phys.* **2008**, *128*, 014104.

(77) Bickelhaupt, F. M.; Baerends, E. J. *Rev. Comput. Chem.* **2000**, *15*, 1–86.

(78) Morokuma, K. *J. Chem. Phys.* **1971**, *55*, 1236–1244.

(79) Kitaura, K.; Morokuma, K. *Int. J. Quantum Chem.* **1976**, *10*, 325–340.

(80) Morokuma, K. *Acc. Chem. Res.* **1977**, *10*, 294–300.

(81) Ziegler, T.; Rauk, A. *Theoret. Chim. Acta* **1978**, *46*, 1–10.

(82) Ziegler, T.; Rauk, A. *Inorg. Chem.* **1979**, *18*, 1558–1565.

(83) Ziegler, T.; Rauk, A. *Inorg. Chem.* **1979**, *18*, 1755–1759.

(84) Frenking, G.; Fröhlich, N. *Chem. Rev.* **2000**, *100*, 717–774.

(85) Frenking, G.; Wichmann, K.; Fröhlich, N.; Loschen, C.; Lein, M.; Frunzke, J.; Rayón, V. M. *Coord. Chem. Rev.* **2003**, *238−239*, 55–82.

(86) The Zn and Ru atoms were described by the $\mathcal{S}$ basis set. For Ru, the core electrons were frozen up to the 3d level.

(87) The largest source of uncertainty in the determination of ΔE_Q most likely comes from the value of the quadrupole moment of the ^{57}Fe $I = 3/2$ excited state. We use the value of $Q = 0.14$ barn determined by Schwerdtfeger et al.,[58] while Pyykkö[88] recommends the value of $Q = 0.16$ barn found by Dufek et al.[89] The 14% difference between these two values provides an estimate of the relative error made in our evaluation of ΔE_Q.

(88) Pyykkö, P. *Mol. Phys.* **2008**, *106* (16−18), 1965–1974, 10.1080/00268970802018367.

(89) Dufek, P.; Blaha, P.; Schwarz, K. *Phys. Rev. Lett.* **1995**, *75*, 3545–3548.

(90) Maruszewski, K.; Strommen, D. P.; Kincaid, J. R. *J. Am. Chem. Soc.* **1993**, *115*, 8345–8350.

(91) Database of Zeolite Structures. http://www.iza-structure.org/databases (accessed Nov 1, 2008).

(92) Meier, W. M.; Olsen, D. H.; Baerlocher, C. *Atlas of Zeolite Structure Types*; Elsevier: London, 1996.

(93) Seidel, S. R.; Stang, P. J. *Acc. Chem. Res.* **2002**, *35*, 972–983.

(94) Fujita, M.; Tominaga, M.; Hori, A.; Therrien, B. *Acc. Chem. Res.* **2005**, *38*, 369–378.

(95) Tranchemontagne, D. J.; Ni, Z.; O'Keeffe, M.; Yaghi, O. M. *Angew. Chem., Int. Ed.* **2008**, *47*, 5136–5147.

(96) Sakai, N.; Matile, S. *Angew. Chem., Int. Ed.* **2008**, *47* (50), 9603–9607, 10.1002/anie.200803300.

(97) Alkordi, M. H.; Liu, Y.; Larsen, R. W.; Eubank, J. F.; Eddaoudi, M. *J. Am. Chem. Soc.* **2008**, *130*, 12639–12641.